Predicting Localized Corrosion in Seawater

N. Sridhar,‡,* C.S. Brossia,* D.S. Dunn,* and A. Anderko**

ABSTRACT

A number of alloys, including stainless steels, aluminum, and nickel-based alloys, are used in seawater for various applications. The localized corrosion of these materials is affected, among other factors, by temperature, microbial activity, chlorination, and flow rate. A predictive model, based on the calculation of repassivation and corrosion potentials, is presented and compared to field experiences of these alloys in seawater systems. An empirical model is used for calculating the repassivation potential of these alloys as a function of seawater composition. A mechanistic model is used for calculating the corrosion potential as a function of oxygen and chlorine concentrations. The parameters for the corrosion potential are derived from tests in flowing natural seawater or synthetic seawater. The model calculations agree with the relative ranking of these alloys in seawater. Limitations of the current model and improvements are suggested.

KEY WORDS: aluminum, localized corrosion, seawater, stainless steel

INTRODUCTION

The geographical variation in the corrosivity of natural seawater results from the variations in the salinity, microbiological activity, dissolved oxygen concentration, and temperature.[1] Discounting the inland seas, such as the Dead Sea, the chloride (Cl^-) concentration of seawater varies from about 5.8 g/kg to about 24 g/kg, the sulfate (SO_4^{2-}) concentration varies from 0.8 g/kg to 3.4 g/kg, and the bicarbonate (HCO_3^-) concentration varies from 0.01 g/kg to 0.2 g/kg.[1] Except in the case of Dead Sea, the sodium to magnesium weight ratio (Na/Mg) remains about 8 in these waters and the sodium to calcium weight ratio (Na/Ca) remains about 26.[1]

Natural seawater is more aggressive than artificially made seawater (by mixing the appropriate compounds found in seawater) or seawater that has been sterilized. It has been argued that the microbial organisms in natural seawater increase the open-circuit potential, a process called ennoblement.[2-3] More recently, Salvago and Magagnin[4-5] observed that the corrosion potential of stainless steel (SS) in seawater had a broad distribution, spanning a range of about 500 mV, although the distribution of the corrosion potential narrowed considerably after prolonged exposure with a mean value of about 400 mV vs saturated calomel electrode (SCE).[4] The mechanism of ennoblement is still under some debate,[4] and recent experiments by Salvago and Magagnin[5] argue that the ennoblement may not necessarily be explained by cathodic depolarization arising from microorganisms, but may involve lowering of passive dissolution kinetics. Lacking a sound theoretical basis for the anodic and cathodic kinetics in natural seawater, calculation of the corrosion potential must use of necessity "apparent" anodic and cathodic parameters.

Temperature and chlorination level can determine the corrosion behavior of SS. In natural seawater, the

Submitted for publication December 2002; in revised form, February 2004.
‡ Corresponding author. E-mail: nsridhar@swri.org.
* Southwest Research Institute, 6220 Culebra Road, San Antonio, TX 78238.
** OLI Systems, 108 American Road, Morris Plains, NJ 07950.

severity of localized attack seems to attain a maximum at approximately 30°C. It also has been reported that the ennoblement is not present in seawater heated above 30°C to 40°C, possibly because of the suppression of microbial activity.[6-7] However, such a shift in the corrosion potential with temperature may be specific to SS.[5] Chlorination is typically used to mitigate biofouling, but also may be effective in reducing microbiologically influenced ennoblement. However, the residual chlorine in the water, if sufficiently high, can act as an oxidant and increase the chances of localized attack. Open-circuit potential measurements by Steinsmo, et al.,[7] on a 22% Cr duplex SS have shown that at a residual chlorine level of 1 ppm, the open-circuit potential is of the order of 600 mV_{SCE}.[7] Shone, et al.,[8] showed that as little as 0.1 ppm residual chlorine was sufficient to kill the microbial slime layer on the surface and minimize crevice attack. They found a minimum in open-circuit potential in flowing seawater at about 0.1 ppm residual chlorine and at a residual chlorine level of 0.8 ppm, the crevice attack of Type 316L (UNS S31603)[(1)] SS decreased significantly. The seawater temperature in their test varied from 7°C to 18°C. At higher temperatures, a lower residual chlorine level may be required to minimize both biofilm formation and localized attack due to chlorine. In chlorinated seawater (with a residual chlorine of 1.0 ppm), the severity of attack increases with temperature, without attaining a maximum. This is because suppression of microbiological activity at higher temperatures is no longer a factor. The high residual chlorine causes a high redox potential,[7] and increasing the temperature then increases the probability of initiation of localized attack. There is no clear guidance in the literature on the residual chlorine level for a given alloy and service condition. Although Type 316L SS suffers pitting and crevice attack in stagnant seawater, a range of pitting and corrosion kinetics has been reported.[9-13] This observed distribution in localized corrosion resistance of Type 316L SS may be related to the distribution in corrosion potential, seawater composition, and other factors.

Empirical studies of pitting resistance of a wide range of SS have shown that their resistance to localized attack can be correlated to a pitting resistance equivalent (PRE). The PRE is typically calculated from the alloy composition as:

$$PRE = (Weight\%Cr) + 3.3x(Weight\%Mo) + 16x(Weight\%N) \quad (1)$$

Streicher[14] examined two series of tests conducted on 45 grades of SS and Ni-based alloys in seawater and ranked the performance of these alloys. In one series of tests performed in gently flowing seawater (0.1 m/s), the alloys that showed no or slight crevice attack generally had a PRE value >38. Type 316L SS (PRE = 25.4) showed extensive crevice attack to a maximum depth of 1.93 mm (77 mils) in 30 days. Type 317L (UNS S31703) SS (PRE = 31.7) also showed extensive crevice attack and pitting to a depth of 1.9 mm. Under essentially stagnant conditions and a longer test duration (two years), Oldfield[15] showed that crevice attack occurred even in alloys with PRE >44. However, the depth of crevice attack was quite small in these alloys. There is also a possibility of excess chlorination in Oldfield's test. Strandmyr and Hagerup[16] reviewed the performance of SS in various offshore systems. They reported adequate performance of SS with a PRE >~40 (typically the 6 wt% Mo SS that also contain 0.2% nitrogen). The PRE can be used to provide a rough ranking of SS for seawater service. However, it is not a predictive tool and the cutoff value of PRE above which an alloy is "immune" to localized corrosion varies with environmental conditions. Furthermore, Equation (1) is only valid for a narrow range of alloying elements. It ignores the effects of other alloying elements, such as Cu and W, and the synergistic effects between Cr and Mo.

Predictive models have been developed for seawater corrosion of SS. There are essentially three types of models:

—Empirical models (including the use of PRE) are based on alloy performance in natural seawater over extended time frames.[14,16]

—Mechanistic models consider the electrochemical reactions within and outside the crevice coupled to the transport of various species to and from the crevice. These models include crevice geometry (critical depth, gap, etc.) as an important variable.[15,17]

—Parametric models calculate parameters (e.g., repassivation and corrosion potentials) that are considered as threshold conditions for initiating stable localized corrosion.[18] These parameters may be abstracted from more detailed mechanistic models.

Empirical models that require extended testing periods can be cost prohibitive, especially in the preliminary stages of a design. Mechanistic models of crevice corrosion, such as that developed by Oldfield,[15] do not adequately account for the considerable effect of potential on crevice corrosion initiation, unless the passive dissolution can be regarded as potential dependent. Additionally, these models need input parameters, such as crevice gap and depth, which are difficult to estimate for real systems.

A parametric model, based on the use of experimentally measured repassivation potentials and calculated corrosion potentials, has been shown to be effective in predicting the long-term performance of alloys in chloride-containing environments.[18] If the

[(1)] UNS numbers are listed in *Metals and Alloys in the Unified Numbering System*, published by the Society of Automotive Engineers (SAE International) and cosponsored by ASTM International.

TABLE 1
Nominal Compositions of the Alloys Investigated

Alloy	wt%								
	Al	Cu	C	Cr	Fe	Ni	Mo	N	Others
UNS A91100	>99.0	0.05 to 0.2	—	—	—	—	—		Si+Fe<0.95
UNS S31603	—	—	<0.03	17	Bal.	12	2.5	—	—
UNS S31254	—	0.75	<0.02	20	Bal.	18	6.25	0.20	Mn<1.0

TABLE 2
Four-Factor Algorithmic Test Design for Measuring Repassivation Potentials of Four Alloys[(A)]

Trial Number	Chloride (g/L)	Sulfate (g/L)	Thiosulfate (g/L)	Temperature (°C)
7	6	3.4	0	23
5	15	3.4	0.8	50
1	24	0.8	0	50
2	6	3.4	0	50
8	24	3.4	0	23
2	6	3.4	0	50
12	6	3.4	0.8	23
8	24	3.4	0	23
10	24	0.8	0.8	23
9	6	0.8	0.8	23
14	6	0.8	0	23
13	24	3.4	0.8	50
5	15	3.4	0.8	50
4	15	0.8	0	23
3	6	0.8	0.8	50
1	24	0.8	0	50
9	6	0.8	0.8	23

[(A)] ASTM "Substitute Ocean Water" was used as the baseline solution. Sodium salts were used to alter anionic concentrations.

open-circuit potential (or corrosion potential) is above the repassivation potential, then localized corrosion initiates. The initiation time depends on the difference between these two potentials and becomes longer as the corrosion potential approaches the repassivation potential.[18] If the open-circuit potential is reduced below the protection potential, the localized attack will be arrested and will not continue. For example, the potential of an alloy can be reduced below the repassivation potential by the application of a cathodic current. Cathodic protection of SS by galvanic coupling to iron or zinc, or through an impressed current system, has been shown to be effective against localized attack in natural seawater.[19-22] The parametric model is examined further in this paper for application to predicting the localized corrosion resistance of several alloys in seawater. UNS A91100 (Al 1100) was considered because aluminized steel has been used as a heat exchanger material in some seawater cooling systems.[23] Type 316L SS and UNS S31254 (Alloy 254SMO) were considered because of their use in many offshore components. However, the modeling approach can be extended to other alloy systems, depending upon the application.

[(2)] ASTM D1141-75, Standard Specification for Substitute Ocean Water, ASTM International, 100 Barr Harbor Drive, West Conshohocken, PA 19428.

EXPERIMENTAL PROCEDURES

Materials and Environments

Three alloys were investigated in this study: Type 316L SS, Alloy 254SMO, and Al 1100. The compositions of the three alloys are shown in Table 1. All samples were polished to 600-grit finish prior to the test, rinsed, degreased in acetone (CH_3COCH_3), dried in air, and weighed. The crevice repassivation samples were contacted with Alloy C276 (UNS N10276) holders for electrical connection outside the solution. Literature survey[1] has indicated that chloride, sulfate, bicarbonate, and magnesium are the most important species in seawater corrosivity. Therefore, these variables, along with temperature, were included in the statistical experimental matrix. The baseline solution was the ASTM "Substitute Ocean Water"[(2)] and the anionic concentrations were varied using sodium salts. The other cations and anions in simulated seawater solutions were maintained at a constant concentration typical of seawater: 5.2 g/L magnesium chloride ($MgCl_2$), 1.16 g/L calcium chloride ($CaCl_2$), 0.695 g/L potassium chloride (KCl), and 0.201 g/L sodium bicarbonate ($NaHCO_3$). The experimental matrix is shown in Table 2. An algorithmic design was used, whereby the factors of interest are defined first and the algorithm searches the factor space for the opti-

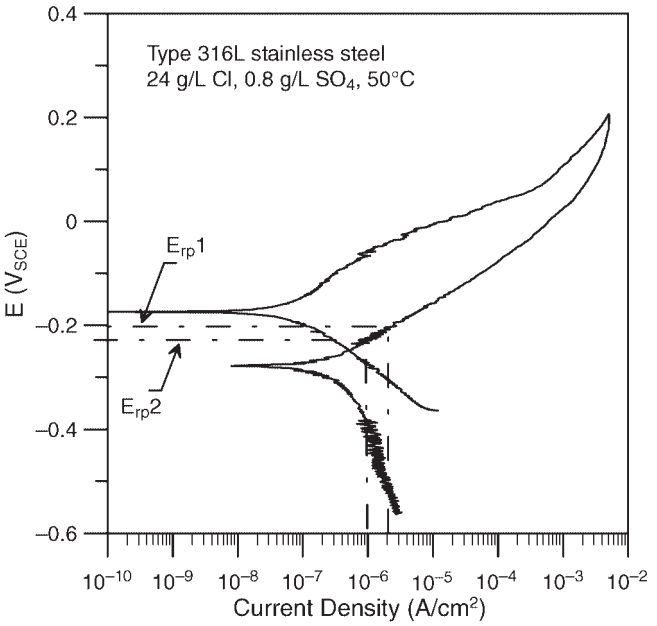

FIGURE 1. *Repassivation potentials measured using CPP tests at a scan rate of 0.167 mV/s.*

mum experimental design. The design includes four linear terms (single factor), three two-way interactions, and one quadratic term for chloride. The matrix also includes five repeats to determine measurement errors and has been randomized to minimize any systematic error.

Repassivation Potential Measurements

The crevice corrosion repassivation potential (E_{rcrev}) was measured. In this paper, the E_{rcrev} and pitting repassivation potential (E_{rp}) are used interchangeably because a previous study has shown that these two potentials are equal within experimental scatter for deep pits.[18] The previous investigation also has shown that such a repassivation potential is a conservative predictor of the long-term occurrence of localized corrosion.[18] Crevices were created on 3-mm-thick (0.125-in.) sheet samples by clamping serrated polytetrafluoroethylene (PTFE) washers (12 teeth per side) using Alloy C276 bolts isolated through PTFE sleeves and an initial torque of 0.14 N-m (20 in. oz).

For alloys UNS S31603 and A91100, cyclic potentiodynamic polarization (CPP) technique at a scan rate of 0.167 mV/s from the open-circuit potential was used to derive the repassivation potentials (Figure 1). The repassivation potentials were defined as the potentials at which the current density corresponded to 2×10^{-6} A/cm^2 ($E_{rcrev}1$ or $E_{rp}1$) or 1×10^{-6} A/cm^2 ($E_{rcrev}2$ or $E_{rp}2$) during the backward scan. For the more corrosion-resistant Alloy 254SMO, such a technique can yield erroneous values of potentials. This is because in a CPP, the current is reversed after attaining a preset value, which in these cases results in attaining high potentials (above 1 V_{SCE}). At these high potentials, although the current is high, there is no observed localized corrosion, only transpassive dissolution. Therefore, if one assumes that the repassivation is the potential at which the reverse scan meets the forward scan or at which the reverse scan attains a specific low current density, a high, but false, repassivation potential is indicated. The fact that a high potential in the forward scan does not initiate localized corrosion is illustrated (Figure 2) using a potentiostatic technique. As shown in Figure 2(a), when the potential is first held at 1.2 V_{SCE} to initiate crevice corrosion and then it is decreased to 0.8 V_{SCE} to propagate crevice corrosion, no crevice corrosion occurred as indicated by a constant current and lack of any visual evidence of corrosion inside the crevices. Indeed, in this case, there was significant corrosion outside the crevice rather than inside, indicating that transpassive dissolution was occurring. In this case, measurement of the potential at which the current decreases to a low value would not yield a true repassivation potential. However, when the initial potential was 1.0 V_{SCE}, then decreasing the potential to 0.8 V_{SCE} subsequently resulted in crevice corrosion growth as indicated by the current increase (Figure 2[b]). Visual observation of specimens in this case indicated that crevice corrosion occurred inside the crevice sites. In this case, decreasing the potential would yield a true repassivation potential.

Tests also were conducted in LaQue Center for Corrosion Technology, Inc. labs (North Carolina) using filtered, natural seawater flown into a laboratory and maintained at 25°C. Duplicate specimens were tested using cyclic potentiodynamic polarization tests at 0.167 mV/s.

Corrosion Potential Measurements

The corrosion potential and the anodic and cathodic kinetics were determined using rotating cylinder electrodes (RCE) and a Pine Instrument model AFMSRX[†] rotator. The samples were 12 mm (0.5 in.) diameter and 8 mm long. Three rotation speeds were used: 100, 1,000, and 10,000 rpm, but all the data reported here were collected using a rotation speed of 1,000 rpm. Tests in simulated seawater were conducted in ASTM D1141 "Substitute Ocean Water" to evaluate the effects of oxygen partial pressure and chlorine concentration. The effect of oxygen was evaluated by continuously sparging ultrahigh-purity nitrogen, nitrogen + 5% oxygen, nitrogen + 21% oxygen, or pure oxygen gases through the test cell fitted with a porous silica frit and an exit trap filled with deionized water. The dissolved oxygen was measured periodically using an Omega Engineering DOH-920[†] dissolved oxygen meter. Direct addition of sodium hypochlorite (NaOCl) into the test cell resulted in a time varying concentration of chlorine. Therefore, chlorine was generated by

[†] Trade name.

electrolyzing the substitute ocean water using platinum electrodes in a separate cell. The chlorinated substitute ocean water then was circulated to the test cell using a peristaltic pump. The test gases were sparged through the chlorine generating cell simultaneously with sparging through the test cell. The chlorine concentration in the test cell was measured using a Hanna Instruments HI 93710† chlorine meter at approximately 2-h intervals. The chlorine meter uses a colorimetric approach in which Hach DPD chlorine reagent (which contains carboxylate salt, sodium phosphate, dibasic, anhydrous potassium iodide, and N,N-diethyl-p-phenylenediamine) is added to a cuvet containing the specimen of interest inducing a color change. The magnitude of the color change is proportional to the chlorine concentration and is measured using the meter.

The current in the electrolyzer was adjusted to obtain a constant residual chlorine level in the test cell. The specimen remained at open-circuit potential for 48 h and the evolution of the corrosion potential was monitored. The corrosion potential increased significantly (sometimes by about 500 mV) and attained a pseudo steady state after about 48 h. Subsequent to this, cathodic polarization was performed at a scan rate of 0.5 mV/s to measure the cathodic Tafel slope and the limiting current. The cathodic scan was stopped at –1.25 V_{SCE}. The anodic polarization was performed on a separate sample in another test cell to measure the anodic Tafel slope. The same hold time (48 h) and scan rate was used for the anodic polarization as for the cathodic polarization measurements in synthetic seawater.

Tests in natural seawater were conducted at LaQue laboratories in North Carolina, using a once-through flowing, filtered seawater in a test tank in which a RCE was rotated at 1,000 rpm. Tests were conducted at 25°C and 35°C, in the latter case with a heater in the test tank. The dissolved oxygen concentration and pH were monitored once a week. The total test duration was 14 days. The dissolved oxygen concentration varied from 6.5 ppm to 7.4 ppm at 25°C and 4.9 ppm to 5.6 ppm at 35°C. The data for 0 days represent those collected immediately after immersion of the specimens in the seawater. The cathodic and anodic polarization tests were conducted on the same specimen, with the cathodic polarization curve being conducted first and the anodic polarization at the end of the cathodic scan from the most cathodic potential.

RESULTS

Crevice Repassivation Potential

The results of the statistically designed experiments on the $E_{rcrev}2$ values in mV_{SCE} are shown for the three alloys in Equations (2) through (4). For Type 316L:

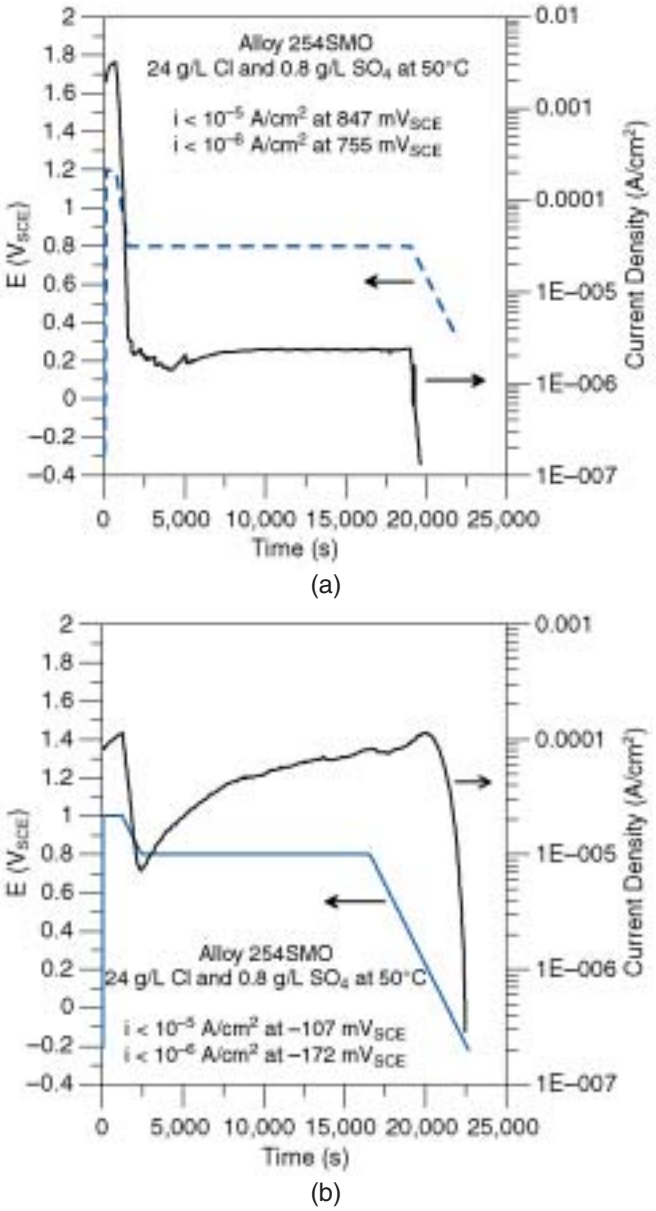

FIGURE 2. *Effect of initiation potential on the repassivation potential of Alloy 254SMO. In case (a), no localized corrosion was initiated, just transpassive dissolution. The current was constant at the lower potential. For case (b), the current at 0.8 V_{SCE} increased indicating localized corrosion.*

$$E_{rcrev}2(316LSS) = -301.5 - 3.7(Cl^- - 15) - 15.3(SO_4^{2-} - 2.1) - 188.7(S_2O_3^{2-} - 0.4) - 2(T°C - 36.5) - 0.047(Cl^- - 15)(SO_4^{2-} - (2.1) + 3.83(Cl^- - 15)(S_2O_3^{2-} - 0.4) - 0.75(Cl^- - 15)(T°C - 36.5) + 0.35(Cl^- - 15)^2 \quad (2)$$

The concentrations of the anionic species in Equation (2) are given in mg/L. The terms on the right side of the equation are centered on their mean values (Table 2). The R^2 for the regression was 0.919 and the root

mean square error (RMSE) was 39.84 mV. Another statistical parameter for testing the significance of a factor is the p-value. The p-value is defined as the probability of obtaining a value for test statistic that is at least as extreme as the observed value assuming that the null hypothesis is true. In other words, if a factor is considered to be significant in affecting the measured parameter (e.g., E_{rcrev}), the probability that the null hypothesis is accepted (i.e., no change in the measured parameter) should be lower than a preselected significance level. Typically, the significance level is chosen as 0.05 (corresponding to a 95% confidence level). If the p-value associated with a factor is <0.05, it is statistically considered to be a significant factor in affecting the measured parameter. The most important factors in Equation (2) were Cl^- and SO_4^{2-} ($p < 0.05$). For Al 1100:

$$\begin{aligned} E_{rcrev}2(\text{All}\,100) = {} & -835.5 + 0.16(Cl^- - 15) + \\ & 1.84(SO_4^{2-} - 2.1) + 23.6(S_2O_3^{2-} - 0.4) - \\ & 1.28(T°C - 36.5) + 1.14(Cl^- - 15)(SO_4^{2-} - 2.1) - \\ & 0.685(Cl^- - 15)(S_2O_3^{2-} - 0.4) - \\ & 0.081(Cl^- - 15)(T°C - 36.5) - 0.042(Cl^- - 15) \end{aligned} \quad (3)$$

The regression coefficient, R^2, was 0.758 and the RMSE was 22.08 mV. Only temperature was important ($p = 0.0178$). The repassivation potentials measured for Al 1100 are consistent with those reported by Furuya and Soga.[24] The results for Alloy 254SMO show that:

$$\begin{aligned} E_{rcrev}2(254\text{SMO}) = {} & +341.4 - 18.8(Cl^- - 15) - \\ & 1.8(SO_4^{2-} - 2.1) - 170.5(S_2O_3^{2-} - 0.4) - \\ & 24.9(T°C - 36.5) + 0.97(Cl^- - 15)(SO_4^{2-} - 2.1) - \\ & 13.2(Cl^- - 15)(S_2O_3^{2-} - 0.4) + \\ & 0.8(Cl^- - 15)(T°C - 36.5) - 1.84(Cl^- - 15) \end{aligned} \quad (4)$$

The R^2 for the regression was 0.979 and the RMSE was 86.2. The most important factors were Cl^- ($p = 0.0001$), temperature ($p = 0.0001$), $Cl^- \times T°C$ ($p = 0.005$), and $S_2O_3^{2-}$ ($p = 0.018$). As expected from its superior performance in seawater, the repassivation potential of Alloy 254SMO was considerably higher than that of Type 316L SS. These results show that over a limited range of seawater compositions, the dependence of the repassivation potentials on environmental factors varies with the alloy. The main utility of the statistically designed experiments is the indication of the important factors for a given alloy. The regression equations (Equations [2] through [4]) are limited by the factorial design chosen. They do not provide truly functional relationships. For example, the regression equation assumes a quadratic relationship to chloride, whereas the true functional relationship may be bi-logarithmic depending on the chloride concentration. To determine the true functional relationship, experiments over several levels of this factor are needed.

The results of duplicate crevice repassivation potential measurements in natural seawater at 25°C are as follows:

—Al 1100: –0.761 V_{SCE}, –0.760 V_{SCE}

—Type 316L SS: –0.177 V_{SCE}, –0.186 V_{SCE}

These values are consistent with those derived from experiments on synthetic seawater (Equations [2] and [3]).

Corrosion Potentials

Results from natural seawater tests are shown in Figures 3 through 5 for Type 316L SS, Al 1100, and Alloy 254SMO, respectively. In all three cases there was a general increase in corrosion potential with time. For UNS S31603 at 25°C, the corrosion potential attained a maximum after about 7 days, whereas at 35°C, the corrosion potential continued to rise to about –0.1 V_{SCE} at the end of the test. However, it appears that at 35°C, the corrosion potential attained a pseudo steady-state value after about 7 days. The changes in corrosion potential at 25°C for this alloy correlate with a decrease in the limiting current density. In the absence of a significant change in dissolved oxygen concentration, this would signify the presence of an anodic film at longer time periods. This is consistent with the changes in the shape of the cathodic polarization curves, especially at 25°C, where a slight inflection in the slope at about –0.4 V_{SCE} is indicative of changes in the location of the real anodic and cathodic curves.[4] For UNS A91100 at 25°C, the corrosion potentials increased from –1.07 V to –0.75 V after 5 days, but seemed to attain a steady state after 2 days. The increase in open-circuit potential with time in seawater is consistent with previously reported results for 99.95% pure aluminum.[25] The transport-limited current density in the current experiments are one order of magnitude lower than those reported by Gundersen and Nisancioglu.[25] This discrepancy may be due to differences in hydrodynamics between the tests. For UNS A91100 at 35°C, the corrosion potentials increased from –1.12 V_{SCE} to –0.82 V_{SCE} after 5 days. Once again, there was a concomitant decrease in the limiting current density. For UNS S31254, the corrosion potential at 25°C did not seem to attain a steady-state value after 14 days, but increased by about 400 mV. At 35°C, the corrosion potential continued to increase after 14 days, but the rate of increase was slow after 7 days, indicating a possible attainment of steady state after this time period. The increase in corrosion potential was about 200 mV after 14 days.

As indicated by Salvagio and Magagnin,[4] these values can have a broad distribution and therefore single specimen values may not provide complete information on the behavior of these alloys in natural seawater. However, comparing the E_{rcrev} of these three

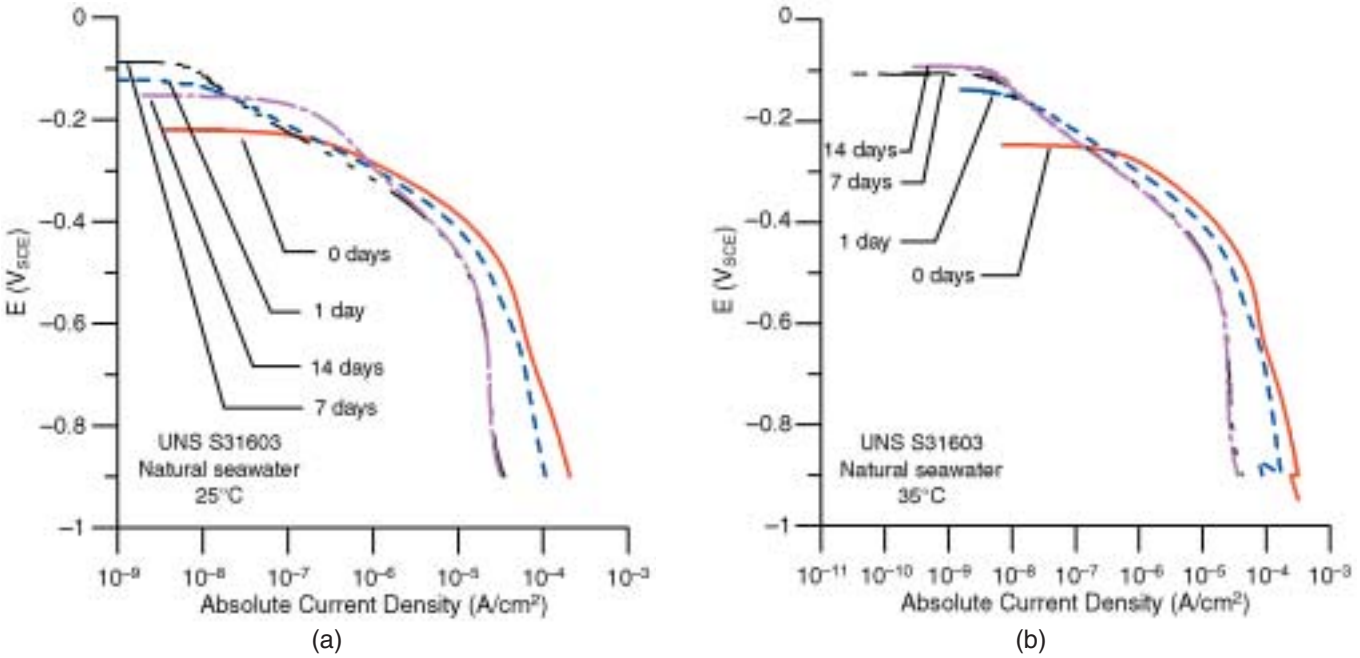

FIGURE 3. *Cathodic polarization curves on UNS S31603 at two different temperatures in natural seawater. RCE at 1,000 rpm.*

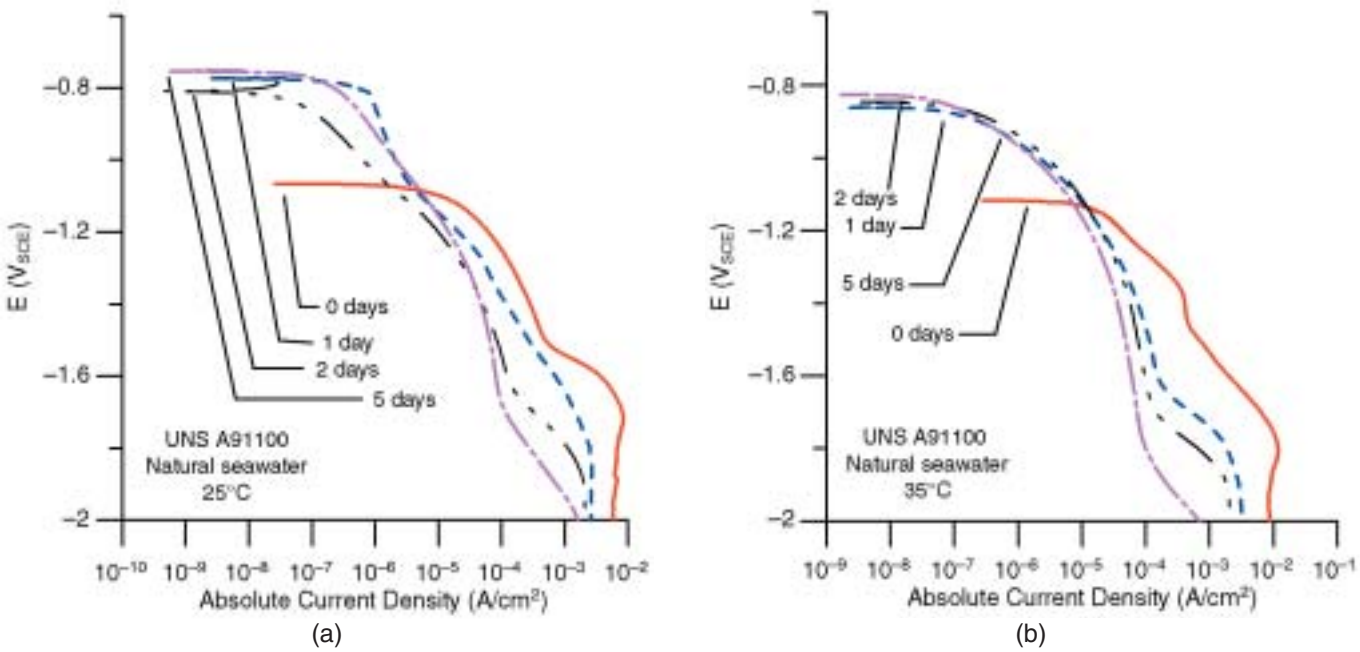

FIGURE 4. *Cathodic polarization curves on UNS A91100 at two different temperatures in natural seawater. RCE at 1,000 rpm.*

alloys (Equations [2] through [4]), the average repassivation potentials of UNS S31603 of –301 mV_{SCE} was more negative than the measured value of corrosion potential (–100 mV_{SCE}) in natural seawater, indicating that this alloy would be expected to suffer crevice corrosion. This is consistent with general seawater experience with this alloy. However, it must be noted[4] that the corrosion potential of this alloy in seawater can be as low as –200 mV. If one assumes that there is a distribution in the E_{rcrev}, and seawater composition has sufficiently low concentrations of aggressive species (Equation [3]), there may be circumstances where the SS may perform adequately. Additionally, in synthetic seawater or seawater that is sterilized, the corrosion potential may be lower than the E_{rcrev}. It must be noted that the pit initiation potential reported

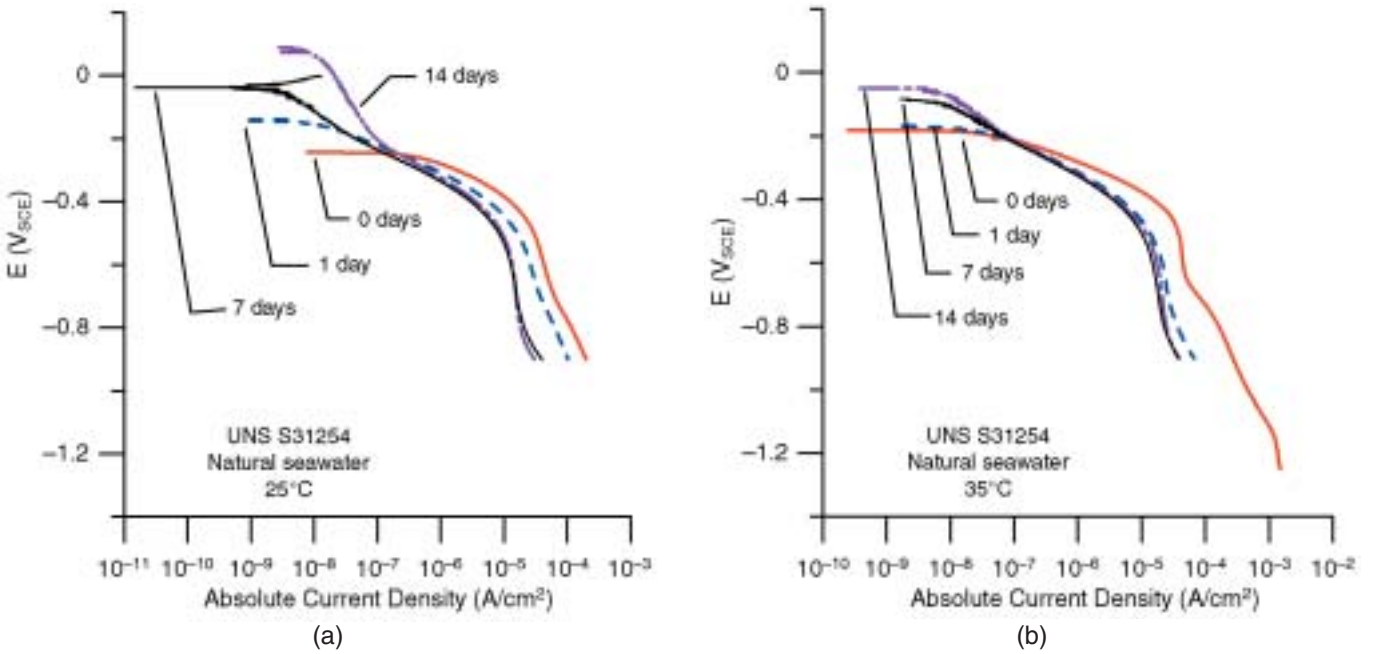

FIGURE 5. *Cathodic polarization curves on UNS S31254 at two different temperatures in natural seawater. RCE at 1,000 rpm.*

for UNS S31603 in natural seawater at 25°C is about 500 mV_{SCE},[22] which is much higher than the measured corrosion potentials for this alloy. Thus, pit initiation potentials are not good estimators of the occurrence of localized corrosion.

The corrosion potential of UNS A91100 (about –750 mV_{SCE}) is slightly more positive than its E_{rcrev}. However, because the corrosion potential is very close to the repassivation potential, it is possible that localized corrosion occurred readily on this alloy and lowered the corrosion potential to a value approximately equal to or only slightly more positive than the repassivation potential, suggesting that under some circumstances the alloy may experience localized corrosion. For UNS S31254, the corrosion potential was at least 300 mV more negative than the E_{rcrev}. This alloy has performed well in seawater service without chlorination.[7]

COMPUTATIONAL MODEL

In this section, we describe a semi-empirical computational model that is designed to reproduce the effects of key independent variables (i.e., aeration, chlorination, temperature, pH, and single-phase flow conditions) on the corrosion potential. Further, the model makes it possible to predict the corrosion potential at conditions that have not been experimentally investigated. When combined with appropriate values of the repassivation potential (Equations [2] through [4]), the model is used to predict the long-term occurrence of localized corrosion as a function of environmental variables.

In previous studies,[26-27] a comprehensive electrochemical model was developed for simulating the general corrosion of metals in complex aqueous environments. This model is also suitable for calculating the corrosion potential for passive metals. The model consists of a thermophysical module and an electrochemical module. The thermophysical module predicts the speciation of the aqueous environment and the activities and transport properties of solution species that participate in interfacial reactions. The electrochemical model utilizes this information to simulate electrochemical reactions at the metal-solution interface. The fundamentals of the thermophysical module are summarized in Appendix A.

The electrochemical model of general corrosion takes into account various partial reactions on the surface of the metal and transport processes for the species that participate in the reactions. The model includes passivation phenomena, which may be influenced by pH and the presence of aggressive or inhibitive species in the solution. Further, it combines the partial processes to compute corrosion rates in the framework of the mixed potential theory. This model was shown to be accurate for simulating the effects of solution chemistry on corrosion rates.[26-27] In this study, we generalize it and apply it to calculate the corrosion potential of aluminum, Type 316L SS, and Alloy 254SMO in seawater. Specifically, we generalize the treatment of anodic dissolution in the passive state so that pH effects on passive current density are accurately predicted and the effect of fluid flow is included for single-phase flow conditions. Also, we focus on developing a semi-empirical treatment of the

oxygen reduction reaction at conditions at which this process is not under mass-transfer control (as is typical for SS).

The model includes expressions for partial anodic and cathodic processes, which may occur under activation or mass-transport control. The expressions are in agreement with the generally accepted views on the mechanisms of partial processes. In the active state, the current density of metal dissolution is given by:

$$i_{Me} = i^0_{Me} \exp\left[\frac{\alpha_{Me} F(E - E^0_{Me})}{RT}\right] \quad (5)$$

where the exchange current density, i^0_{Me}, incorporates the effect of adsorption of species and is related to the activities of solution species as described in previous papers.[26-27] The reversible potential, E^0_{Me}, is defined on the basis of the Nernst equation for the most abundant metal in the alloy. This approach is necessary in view of the fact that the Nernst equation can be defined solely for a single redox couple (i.e., a metal/metal ion couple). As long as selective dissolution of alloy components is neglected (which is a safe approximation for the metals studied here), this approach does not introduce any error.

The active-passive transition is introduced into the electrochemical model by considering a current that leads to the formation of a passive layer in addition to the current that leads to active dissolution. At any instant, a certain fraction of the surface, θ_P, is assumed to be covered by a passive layer. The change of the passive layer coverage fraction with time can be expressed as:[26]

$$\left(\frac{\partial \theta_P}{\partial t}\right)_{E,a_i} = c i_{MeO}(1 - \theta_P) - K\theta_P \quad (6)$$

where i_{MeO} is the current density that contributes to the formation of a passive layer. The second term on the right-hand side of Equation (6) represents the rate of dissolution of the passive layer, which is proportional to the coverage fraction. Solution of this equation in the steady-state limit yields an expression for the anodic dissolution current:

$$i_{Me,TOT} = \frac{i_{Me} + i_{MeO}}{1 + \frac{c i_{MeO}}{K}} = \frac{i_{Me} + i_{MeO}}{1 + \frac{i_{MeO}}{i_P}} \quad (7)$$

where i_{Me} is the dissolution current density in the active state and the ratio $i_p = c/K$ constitutes the passive current density. This formulation can represent the observable characteristics of the active-passive transition as demonstrated in a previous paper.[27]

For calculating the corrosion potential, the quantitative modeling of passive dissolution is of primary importance. In the absence of specific active ions, the passive current density depends primarily on the pH of the solution. For acidic solutions, we consider a dissolution reaction between the passive oxide/hydroxide surface layers and protons from the solution, i.e.:

$$\equiv MeO_a(OH)_b + (2a + b - x)H^+ = Me(OH)_x^{(2a+b-x)+} + (a + b - x)H_2O \quad (8)$$

where the symbol "≡" denotes surface species. The corresponding kinetic equation is:

$$i_{p,H^+} = k_{H^+} a^{*s}_{H^+} \quad (9)$$

where $a^{*s}_{H^+}$ denotes the surface concentration of hydrogen ions and s is a reaction order, which is not necessarily related to the stoichiometric coefficient in the dissolution reaction.

In neutral solutions, the predominant dissolution reaction is:

$$\equiv MeO_a(OH)_b + aH_2O = Me(OH)^0_{(2a+b),aq} \quad (10)$$

where the predominant species on the right-hand side of Equation (10) is a neutral complex as indicated by the superscript 0. The corresponding kinetic equation is:

$$i_{p,H_2O} = k_{H_2O} a^{*u}_{H_2O} \quad (11)$$

where the reaction order with respect to water indicates that dissolution may be affected by water activity. Such effects may be observed primarily in concentrated solutions, in which water activity differs from one. Similarly, the predominant reaction in alkaline solutions is:

$$\equiv MeO_a(OH)_b + (x - 2a - b)OH^- + aH_2O = Me(OH)_x^{(x-2a-b)-} \quad (12)$$

with a corresponding kinetic equation given by:

$$i_{p,OH^-} = k_{OH^-} a^{*v}_{OH^-} \quad (13)$$

The total passive current density as a function of pH is given by:

$$i_p = i_{p,H^+} + i_{p,H_2O} + i_{p,OH^-} \quad (14)$$

The kinetic equations can be rewritten in terms of bulk concentrations of ions by considering the mass-transfer equation:

$$\frac{i_{p,i}}{zF} = k_m(a_i - a^*_i) \quad (15)$$

where k_m is a mass-transfer coefficient and a_i is the bulk activity of the reacting species. The mass-transfer coefficient can be computed for various flow regimes as described in a previous paper.[27] Then, the surface concentration, a_i^*, can be obtained from Equation (15) and substituted into Equations (9), (11), or (13). For example, in the case when v = 1, Equation (13) can be expressed in a closed form as:

$$\frac{1}{i_{p,OH^-}} = \frac{1}{k_{OH^-} a_{OH^-}} + \frac{1}{k_m z F a_{OH^-}} \quad (16)$$

The relative importance of the two terms on the right-hand side of Equation (16) depends on the particular system. As demonstrated previously (e.g., Kaesche,[28] Craig and Scott[29]), the anodic dissolution of aluminum in alkaline solutions may be partly under mass-transport control. However, there is no substantial evidence for the mass-transfer effects on the anodic dissolution of SS under typical conditions such as those in seawater. In such cases, the second term on the right-hand side of Equation (16) becomes negligible.

In addition to pH effects, some active ions may influence the magnitude of the passive current density. The effect of active species on the dissolution in the passive state can be modeled by considering surface reactions between the metal oxide film and solution species, i.e.:

$$\equiv MeO_a(OH)_b + c_i X_i = \equiv MeO_a(OH)_b X_{c_i} + e_i OH^- \quad (17)$$

where X_i is the i-th reactive species in the solution and a, b, c_i, and e_i represent the reaction stoichiometry. In Equation (17), the stoichiometry is usually difficult to define because of the dynamic nature of the system and may be, in general, fractional. In general, Equation (17) may be written for any active, aggressive, or inhibitive species i in the solution (i = 1, …, n). It is reasonable to assume that Equation (17) is in quasi-equilibrium and it can be characterized by an equilibrium constant. The surface species that forms as a result of Reaction (17) may undergo irreversible dissolution reactions such as:

$$\equiv MeO_a(OH)_b X_{c_i} + aH_2O \rightarrow Me(OH)^0_{2a+b,aq} + c_i X_i \quad (18)$$

in which dissolved metal species are formed in analogy to those described by Equations (8), (10), and (12). Mathematical analysis of Reactions (17) and (18)[26] yields a relationship between the passive current density and activities of reactive species, i.e.:

$$i_p = i_p^0(pH) \frac{1 + \sum_i l_i \frac{a_{X_i}^{c_i}}{a_{OH^-}^{e_i}}}{1 + \sum_i K_i \frac{a_{X_i}^{c_i}}{a_{OH^-}^{e_i}}} \quad (19)$$

where $i_p^0(pH)$ is given by Equation (14), l_i is the forward rate of Reaction (18), and K_i is the equilibrium constant of Reaction (17).

In seawater systems, typical partial cathodic processes include the reduction of dissolved oxygen, water molecules, carbonic acid ($[H_2CO_3]$ which is formed from dissolved carbon dioxide $[CO_2]$), and hypochlorite ions (ClO^-), which result from chlorination treatments. In aerated systems, the reduction of dissolved O_2 is usually the most important cathodic reaction, i.e.:

$$O_2 + 4H^+ + 4e^- \rightarrow 2H_2O \quad (20)$$

In general, the oxygen reduction reaction may follow a complex mechanism. The mechanism of oxygen reduction on SS was analyzed by Le Bozec, et al.,[30] and in papers cited therein. It has been established that the reaction may proceed either through a four-electron pathway, which leads to the reduction of O_2 to H_2O, or through a two-electron pathway, which leads to the formation of hydrogen peroxide (H_2O_2) as an intermediate. The reaction pathway is influenced by many factors such as the surface treatment of the electrode. A detailed investigation of the oxygen reduction mechanism is outside the scope of this study since the measurement of cathodic polarization curves alone is insufficient to elucidate the mechanism. Instead, we focus on determining the parameters that control the value of the corrosion potential as a function of dissolved oxygen concentration and pH. These parameters include the electrochemical transfer coefficient and the reaction orders with respect to dissolved oxygen and protons. Once these parameters are determined using experimentally measured corrosion potentials and Tafel slopes, the oxygen reduction reaction can be modeled on a semi-empirical basis. The oxygen reduction process is subject to mass-transfer limitations, due to the diffusion of dissolved oxygen molecules. Thus, the expression for the current density for oxygen reduction can be expressed as:

$$\frac{1}{i_{O_2}} = \frac{1}{i_{O_2,a}} + \frac{1}{i_{O_2,lim}} \quad (21)$$

where:

$$i_{O_2,a} = i^*_{O_2} a^q_{O_2} a^r_{H^+} \exp\left[\frac{-\alpha_{O_2} F (E - E^0_{O_2})}{RT}\right] \quad (22)$$

$$i_{O_2,lim} = 4 k_m F a_{O_2} \quad (23)$$

The reaction orders q and r in Equation (22) are, in general, specific to the metal surface, although they are expected to be similar within families of alloys. On the other hand, the diffusion-limited current density (Equation [23]) is practically independent of the surface because the mass-transfer coefficient depends

only on flow conditions, diffusivity of oxygen, and density and viscosity of the solution. In this study, the reaction orders are determined from experimental data as outlined above and the limiting current densities are predicted for simple single-phase flow regimes as described in previous papers.[26-27] Thus, the limiting current densities are not adjusted using experimental data. For the calculation of the corrosion potential on SS, Equation (22) plays the most important role since oxygen reduction on passive surfaces does not proceed under straightforward mass-transfer control. Equation (22) is treated as a semi-empirical expression in which the constant $i^*_{O_2}$ and the reaction orders q and r are calibrated to match experimental data.

Another cathodic reaction is the reduction of water molecules, which predominates in deaerated systems:

$$H_2O + e^- \rightarrow 0.5H_2 + OH^- \quad (24)$$

Unlike the reduction of oxygen, the water reduction does not exhibit a limiting current density because there are no diffusion limitations for the transport of H_2O molecules to the surface. Thus, the current density can be expressed as:

$$i_{H_2O} = i^0_{H_2O} \exp\left[\frac{-\alpha_{H_2O}F(E - E^0_H)}{RT}\right] \quad (25)$$

where the reversible potential, E^0_H, is calculated from the Nernst equation and:

$$i^0_{H_2O} = i^*_{H_2O} a^q_H a^r_{H_2O} \quad (26)$$

In chlorinated systems, the reduction of hypochlorite ions plays a significant role:

$$ClO^- + 2H^+ + e^- \rightarrow Cl^- + H_2O \quad (27)$$

or:

$$HClO_{aq} + H^+ + e^- \rightarrow Cl^- + H_2O \quad (28)$$

Since this reaction occurs under combined activation and mass-transport control,[31-32] the expression for its rate is analogous to that for the reduction of oxygen (Equations [21] and [23]).

The parameters of the electrochemical model are determined by utilizing a large number of experimental polarization and corrosion rate data. The partial electrochemical processes described above are combined into a total predicted polarization curve. Then, the corrosion potential is calculated by applying the mixed-potential theory, i.e.:

$$\sum i_{c,i} = \sum i_{a,j} \quad (29)$$

where $i_{c,i}$ and $i_{a,j}$ denote the i-th cathodic and j-th anodic processes, respectively. The electrochemical parameters of the model are determined in a multi-step procedure, i.e.:

- —The kinetic rate constants for calculating the passive current density (Equation [14]) are obtained from experimental current densities for passive dissolution as a function of pH.
- —The exchange current density and electrochemical transfer coefficient for anodic dissolution of the metal in the active state (Equation [5]) is obtained from corrosion rate data and polarization curves for the active dissolution in acidic environments (for SS).
- —The exchange current density and electrochemical transfer coefficient for the reduction of water molecules (Equations [25] and [26]) are obtained from corrosion potential measurements and cathodic polarization curves in deaerated solutions. These parameters play a minor role in typical aerated seawater systems, but are necessary to establish a baseline for deaerated systems.
- —The exchange current density and electrochemical transfer coefficient for the reduction of hydrogen ions are determined from corrosion rate data in acidic solutions. These parameters are of minor importance for seawater systems, but are included for completeness.
- —For the reduction of oxygen molecules (Equations [21] and [22]), the exchange current density, reaction order with respect to dissolved oxygen, and electrochemical transfer coefficient are established on the basis of corrosion potential data and cathodic polarization curves in solutions with various levels of dissolved oxygen.
- —Similarly, analogous parameters for the reduction of ClO^- ions and HClO are obtained from corrosion potential measurements in chlorinated systems.

In this procedure, both literature data and measurements obtained in this study have been utilized. The data sources are described in the next section.

MODELING RESULTS

The model has been validated first for the computation of the corrosion potential using the data obtained in this study as well as various literature sources that cover wide ranges of pH and aeration. Then, the corrosion potential model was applied in conjunction with the repassivation potential data (Equations [2] through [4]) to analyze the conditions that are conducive to localized corrosion in seawater systems. It must be noted that, for the corrosion potential model, only the experimentally measured corrosion potentials for a limited set of experiments are used to calibrate the model. The other parameters are

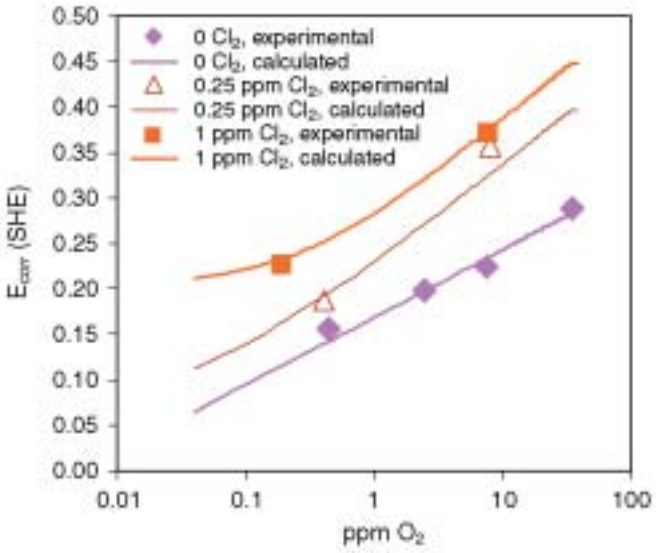

FIGURE 6. *Experimental and calculated corrosion potentials of Type 316L SS in artificial seawater (RCE, 1,000 rpm) as a function of oxygen concentration for three concentrations of dissolved chlorine (i.e., 0, 0.25, and 1 ppm Cl_2).*

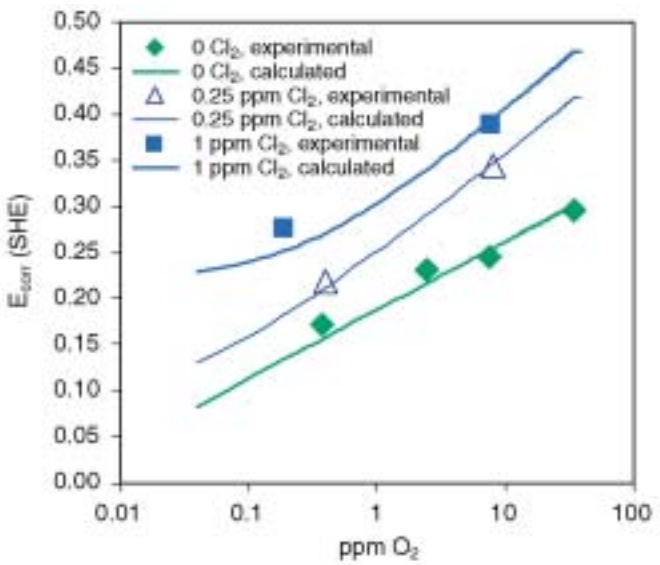

FIGURE 7. *Experimental and calculated corrosion potentials of Alloy 254SMO SS in artificial seawater (RCE, 1,000 rpm) as a function of oxygen concentration for three concentrations of dissolved chlorine (i.e., 0, 0.25, and 1 ppm Cl_2).*

adjusted to fit the limited corrosion potential data and then are used to predict the corrosion potentials under other conditions. The Tafel slopes assumed in the model for fitting the experimental corrosion potential data were found to be in general agreement with the experimentally measured Tafel slopes.

In a previous paper,[33] the general corrosion model was applied to SS in acids. In this study, it was calibrated further to reproduce the corrosion potentials in aerated and chlorinated seawater. In the case of aerated seawater, the corrosion potential is determined by the cathodic process of oxygen reduction (Equations [20] through [23]) and by the passive current density (Equation [14]). For SS in artificial seawater, the passive current density is practically independent of pH and is only a function of temperature. Thus, the dependence of the corrosion potential on the level of aeration and/or chlorination is determined primarily by the kinetics of oxygen and hypochlorite ion reduction on the passive metal surface (Equation [22]).

Figures 6 and 7 show the experimental and calculated corrosion potentials in aerated and chlorinated artificial seawater for Type 316L SS and Alloy 254SMO, respectively. In all cases, the experimental data are accurately reproduced by the model. It is evident from these figures that the dependence of the corrosion potential on the concentrations of dissolved oxygen and chlorine is very similar for both alloys. On average, the corrosion potentials are higher for Alloy 254SMO by about 23 mV (with differences ranging from 7 mV to 49 mV) at identical conditions. This is due to the fact that the mechanism of oxygen reduction on passive surfaces dominated by chromium oxide should be practically identical. The differences in the corrosion potentials for both alloys are accounted for by the differences in their passive current densities. In the model, the passive current density of Alloy 254SMO in seawater at room temperature is smaller than that of Type 316L SS by a factor of 1.45, which quantitatively accounts for the small differences in the corrosion potential. This difference in the passive current densities is reasonable in view of the fact that 254SMO is more highly alloyed.

In the case of aerated seawater without dissolved chlorine, a linear dependence of the corrosion potential on the concentration of dissolved oxygen is observed (Figures 6 and 7). This makes it possible to derive a reaction order with respect to dissolved oxygen concentration from experimental data. It has been determined that a reaction order of approximately 0.5 reproduces experimental data within experimental uncertainty.

Thus, as shown in Figures 6 and 7, the corrosion potential declines relatively slowly as the concentration of dissolved oxygen is lowered from a level that corresponds to contact with pure oxygen (ca. 34 ppm) to a level that results from contact with commercial-purity nitrogen (ca. 0.4 ppm). The addition of small amounts of dissolved chlorine appreciably increases the corrosion potential. The elevation of the corrosion potential results from the superposition of the cathodic reactions of oxygen and hypochlorite reduction. Therefore, the corrosion potential is no longer a linear function of oxygen concentration once a nonzero amount of chlorine is present in the solution (Figures 6 and 7). In solutions containing 1 ppm Cl_2, the presence of chlorine increases the corrosion potential by 120 mV to 180 mV, depending on the concentration of dissolved oxygen.

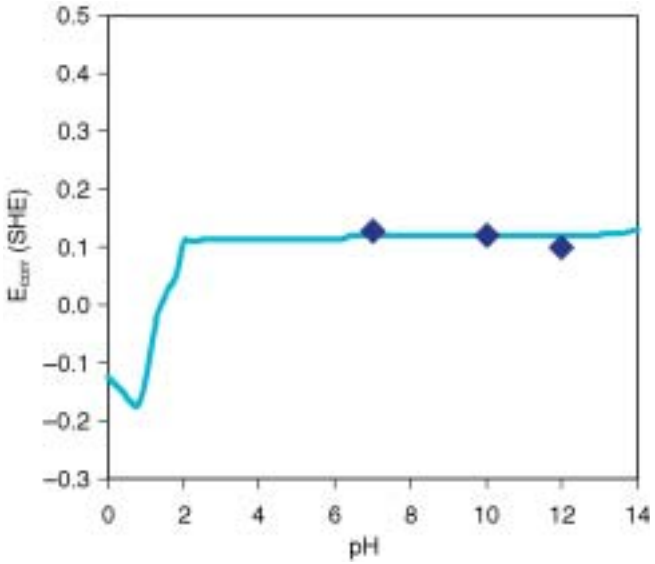

FIGURE 8. *Experimental and calculated corrosion potentials of Type 316L SS in 0.5 m sodium sulfate (Na_2SO_4) solutions with 0.32 ppm O_2 as a function of pH (RCE, 1,000 rpm).*

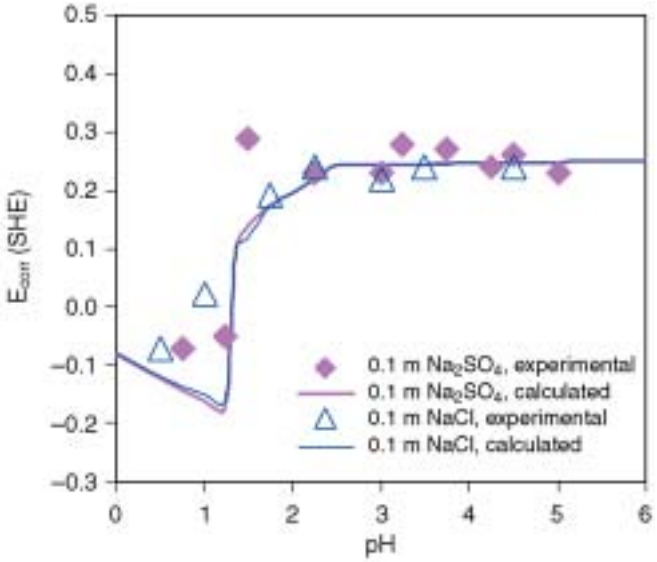

FIGURE 9. *Effect of pH on the corrosion potential of Type 304 SS in aerated 0.1 m Na_2SO_4 or sodium chloride (NaCl) solutions. The symbols denote the experimental data of Leckie,[34] and the lines have been calculated from the model.*

In addition to the effect of dissolved oxygen and chlorine concentration, it is also worthwhile to examine the effect of pH on the corrosion potential. Figure 8 compares the calculated and experimental corrosion potentials for Type 316L SS as a function of pH in 0.5 M sulfate solutions. In the passive range, the corrosion potential is practically independent of pH. It becomes substantially lower when pH is reduced below the depassivation pH. To examine the depassivation pH further, the model also was compared with the data of Leckie[34] for Type 304 (UNS S30400) steel in both sulfate and chloride solutions. As shown in Figure 9, the model reproduces the corrosion potential in both the passive and active ranges. At the same time, the depassivation pH is accurately predicted. Since the depassivation pH is quite low for more corrosion-resistant alloys, Figure 10 examines the corrosion potential of Alloy 254SMO as a function of hydrochloric acid (HCl) concentration rather than pH. In this case, the model predictions are compared with experimental data from this study in neutral solutions (i.e., for $m_{HCl} = 0$) and with literature data[35] in HCl-containing solutions. This demonstrates that the effect of acidity on the corrosion potential (E_{corr}) is correctly reproduced.

Unlike SS, aluminum shows a substantial dependence of the passive current density on the pH of the solution. Also, the passive current density is affected by hydrodynamic conditions because the dissolution of aluminum is partially controlled by the transport of hydroxide ions to the corroding surface.[28-29] The model has been calibrated for aluminum to reproduce both corrosion rate and corrosion potential data in wide pH ranges. The reproduction of steady-state corrosion rate data ensures that the passive current density is

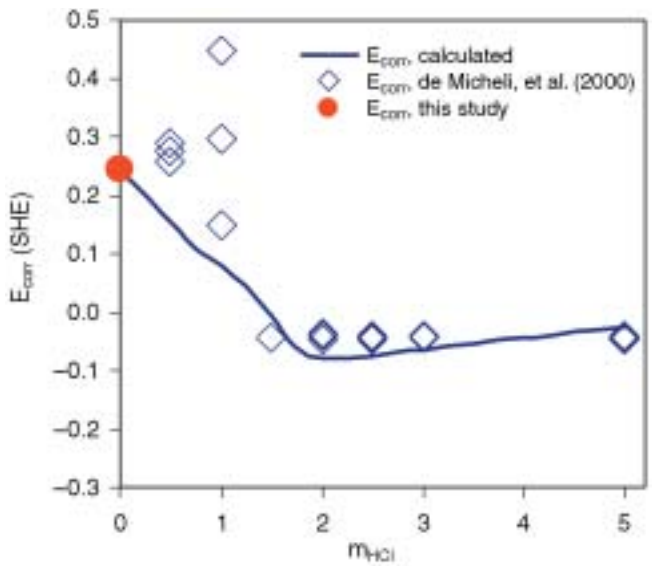

FIGURE 10. *Effect of acidity on the corrosion potential of Alloy 254SMO SS in aerated solutions. The symbols denote the experimental data obtained in this study for neutral solutions and those of de Micheli, et al.,[35] for HCl solutions. The lines have been calculated from the model.*

accurately predicted. The parameters for the reduction partial processes (e.g., the reduction of oxygen) were calibrated to match corrosion potential data in solutions that do not cause localized corrosion (e.g., sulfate or deaerated chloride solutions).

To validate the model for aluminum, deaerated solutions were considered first. Figure 11 shows the effect of flow conditions on the corrosion potential and current density in weakly alkaline solutions

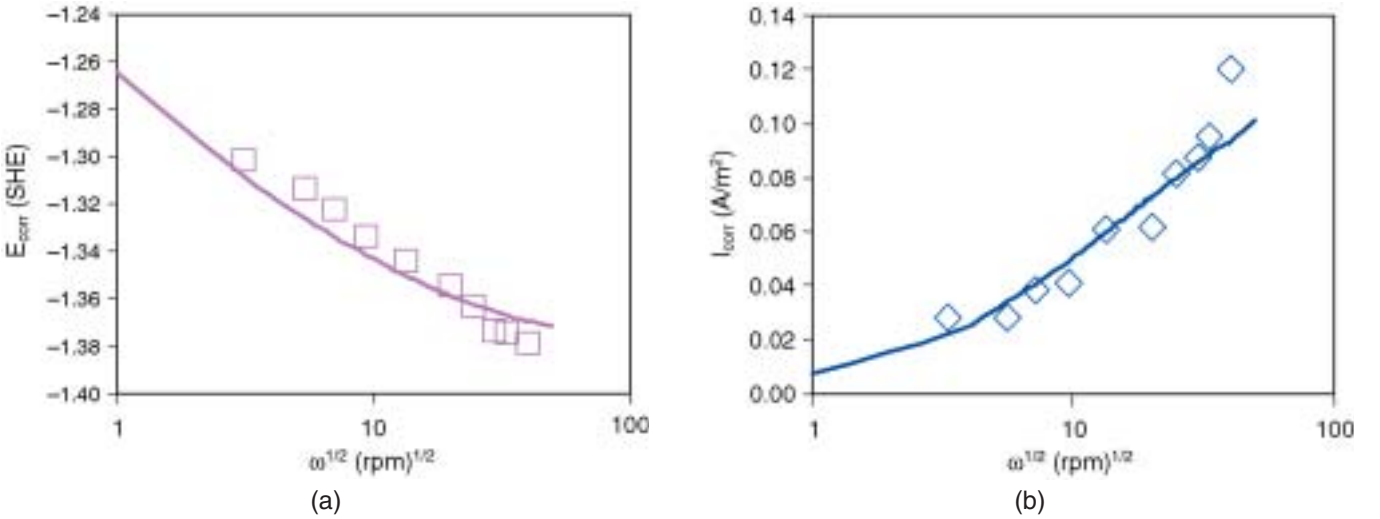

FIGURE 11. *Calculated corrosion potential (left diagram) and corrosion rate (right diagram) for aluminum in a deaerated NaCl solution with pH = 9.02 as a function of the rotation speed of a rotating disk electrode. The symbols denote the experimental data of Craig and Scott.*[29]

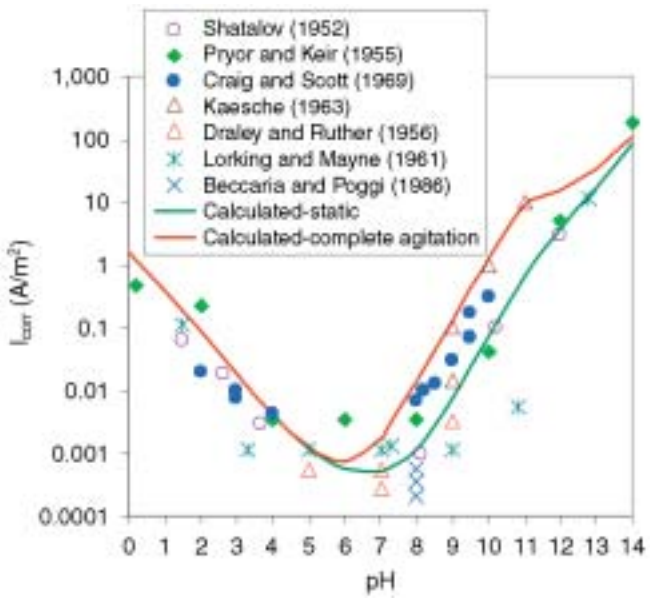

FIGURE 12. *Calculated and experimental corrosion rates of aluminum as a function of pH. The calculated values were obtained for two extreme hydrodynamic conditions, i.e., static and completely agitated solutions. Experimental data were obtained from previous studies.*[28-29,53-57]

(somewhat more alkaline than seawater). The model has been compared with the experimental results of Craig and Scott,[29] which were obtained using a rotating disk electrode in deaerated chloride solutions. The results are shown in Figure 11 for both the corrosion potential and corrosion rate. The experimental data are reproduced with good accuracy. Because the solutions were deaerated, the measured data reflect only general corrosion and are not affected by localized corrosion. It is evident that flow conditions have only a modest effect, in absolute terms, on the corrosion potential. They are more significant for the corrosion rate, for which an increase by a factor of approximately five is observed as the rotation rate is increased.

Figure 12 shows the current density for general corrosion of aluminum as a function of pH in systems, in which localized corrosion does not contribute to the observed dissolution rates. These calculations are useful primarily to validate the magnitude of the predicted passive current density as a function of pH in near-neutral solutions. Since corrosion rates in alkaline solutions are significantly affected by flow conditions, calculations have been made for two extreme flow conditions, i.e., static and completely agitated solutions. The experimental data, which were usually reported without specifying the flow conditions (with the exception of the data of Craig and Scott[29]), are in most cases bracketed by the predictions for static and completely agitated conditions.

Figure 13 shows the calculated corrosion potentials for aluminum in aqueous solutions that do not cause localized corrosion (i.e., primarily in sulfate solutions with varying pH and hydroxide solutions). In near-neutral solutions, the corrosion potentials reflect the reduction of oxygen on a passive surface. It is noteworthy that the corrosion potential strongly depends on pH. The magnitude of the corrosion potential in such systems depends on the electrochemical characteristics of the oxygen reduction reaction (i.e., the electrochemical transfer coefficient and the reaction orders with respect to dissolved oxygen and protons) and on the magnitude of the passive current density. A good agreement with experimental data has been found by setting the transfer coefficient, α, equal to 0.5 and the reaction orders with respect to O_2 and H^+ equal to 0.6 and 1, respectively. A substantial

change in the corrosion potential is observed in the pH range that corresponds to seawater (i.e., between 7.5 and 8.5). This change is primarily due to an increase in the passive current density with increasing alkalinity of the solution. Also, it is influenced by the pH dependence of the oxygen reduction reaction.

After validating the electrochemical model for calculating the corrosion potential, the model has been combined with repassivation potential data (Equations [2] through [4]) to predict the long-term occurrence of localized corrosion. Such analyses are shown in Figures 14 through 21 for various metal-environment combinations. Figures 14 through 21 show predicted current density vs potential diagrams, which have been obtained from the general corrosion model. The dotted lines in these figures represent the partial cathodic and anodic processes that have been taken into account in the model (e.g., oxidation of the metal, reduction of oxygen, hypochlorite ions, water molecules, etc.) The partial processes are labeled with numbers in the figures and are explained in a legend below the diagram. The total current density-potential relationship, or a predicted polarization curve, is shown as a solid line. It should be noted that the calculated polarization curve reflects a hypothetical steady-state behavior, which corresponds to an infinitely slow potential sweep. With this assumption, the breakdown potential on the anodic branch of the polarization curve corresponds to the repassivation potential. This prediction often will differ from an experimental polarization curve, in which the breakdown potential is usually higher than the repassivation potential and depends on the sweep rate and other experimental conditions. The calculated corrosion potential is marked by the symbol "x" on the diagrams. Since the corrosion potential reflects the reduction-oxidation phenomena on the passive surface, the symbol "x" always lies on the vertical portion of the anodic line, which corresponds to passive dissolution. In Figures 14 through 21, the calculated corrosion potential is compared with the experimental values of the corrosion and repassivation potentials at the same conditions. The calculated repassivation potential in Figures 14 through 21 is, by definition, equal to the experimental value (within the range of accuracy of the correlation equations) because the experimental E_{rp} data were used directly in the model. However, the calculated corrosion potential does not reflect a specific single experiment. Instead, it has been calculated using electrochemical parameters that were obtained by reconciling a large body of experimental information.

Figure 14 shows the results of calculations for Type 316 SS in air-saturated seawater at room temperature. The calculations were made for a rotating cylinder electrode with a diameter of 1.2 cm and a rotation rate of 1,000 rpm. As shown in Figure 14, the corrosion potential is determined in this case by the

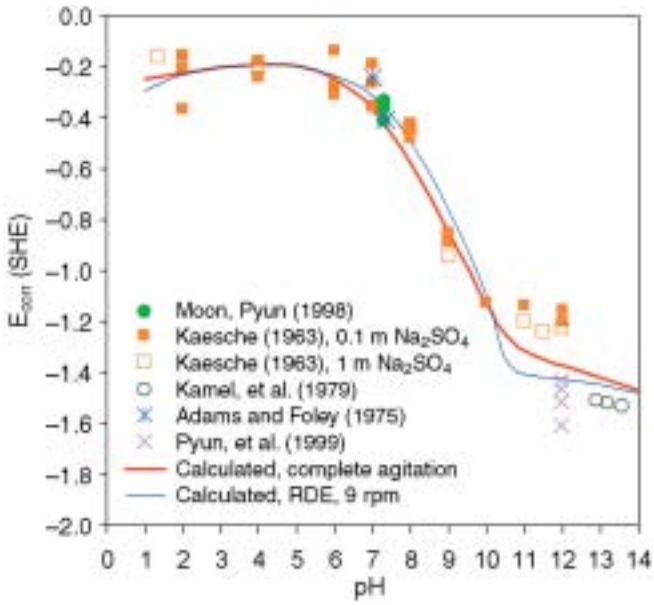

FIGURE 13. *Corrosion potential of aluminum in aerated solutions that do not cause localized corrosion (i.e., aqueous Na_2SO_4 or sodium hydroxide [NaOH]) as a function of pH. The calculations have been made for two hydrodynamic conditions, i.e., for slowly flowing (RDE, 9 rpm) and completely agitated solutions. Experimental data was obtained elsewhere.*[28,58-61]

intersection of the line that corresponds to the reduction of oxygen (labeled by D) with the line that depicts the passive dissolution of the alloy (labeled by E). The remaining partial processes (i.e., the reduction of water, carbonic acid, and protons) are insignificant in this system. The experimental steady-state corrosion potential in aerated seawater is shown as a square. The calculated corrosion potential (marked by an "x") is in excellent agreement with experimental data in artificial seawater. The experimental corrosion potential in natural seawater, which is shown as a triangle, lies slightly below the calculated corrosion potential. The repassivation potential is shown as a rectangle labeled "E_{rp}." It is evident that the repassivation potential is substantially below the corrosion potential, which indicates a tendency for localized corrosion. This is in agreement with the experimentally observed tendency of Type 316L SS to suffer localized corrosion in both natural and artificial seawater environments.

It is of interest to examine the effect of a reduction in the concentration of dissolved oxygen on the tendency of the metal to undergo localized corrosion. Figure 15 illustrates the predicted behavior of Type 316L SS in seawater containing 0.44 ppm of dissolved oxygen. This level of dissolved oxygen corresponds roughly to seawater in contact with commercial-purity nitrogen. Other conditions remain the same as in Figure 14. As shown in Figure 15, the reduction in dissolved oxygen concentration results in a decrease in the calculated corrosion potential and the limiting current density for oxygen reduction. The calculated

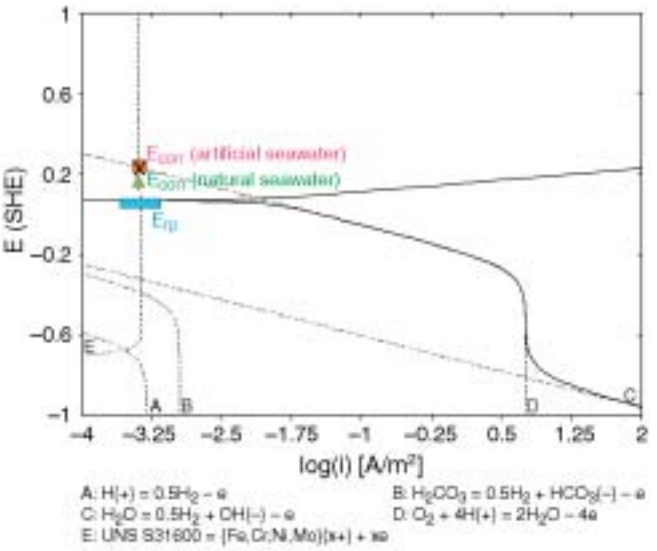

FIGURE 14. *Calculated current density vs potential relationship for Type 316L SS in aerated seawater (7.55 ppm of dissolved O_2, rotation rate 1,000 rpm) at 25°C. The dotted lines labeled A through E show the partial electrochemical processes that were taken into account in the model. The calculated corrosion potential is shown by the "x" symbol. The square and triangle show the experimental corrosion potentials in artificial seawater (7.55 ppm O_2) and natural seawater (6.8 ppm O_2), respectively. The experimental repassivation potential is shown as a rectangle labeled E_{rp}.*

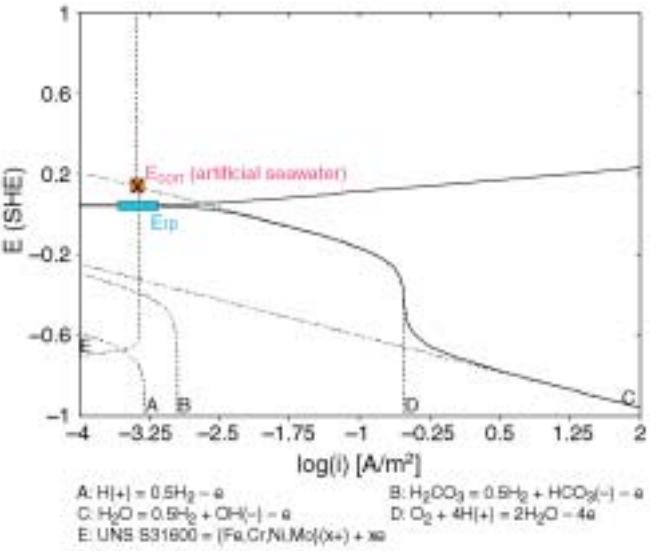

FIGURE 15. *Calculated current density vs potential relationship for Type 316L SS in seawater containing 0.44 ppm of dissolved O_2 at 25°C (rotation rate 1,000 rpm). The dotted lines labeled A through E show the partial electrochemical processes that were taken into account in the model. The calculated corrosion potential is shown by the "x" symbol. The square shows the experimental corrosion potential in artificial seawater. The experimental repassivation potential is shown as a rectangle labeled E_{rp}.*

corrosion potential is in good agreement with the experimental value for artificial seawater. The repassivation potential remains the same because it is affected only by the ionic solution components. The calculated corrosion potential is, however, still above the repassivation potential. This indicates that the system is likely to undergo localized corrosion even when the concentration of dissolved oxygen is reduced to 0.44 ppm. The corrosion potential would become equal to the repassivation potential if the dissolved oxygen concentration was reduced below approximately 0.06 ppm.

Figure 16 shows the results obtained for Alloy 254SMO in aerated seawater at 25°C (i.e., for the same conditions as those shown in Figure 14). In this case, the calculated corrosion potential is very similar to that predicted for Type 316L SS (Figure 14). The calculated corrosion potential closely agrees with the experimental result for artificial seawater (cf. the square in Figure 16) and is slightly above the potentials obtained in natural seawater (cf. the triangles). However, the repassivation potential has a substantially higher value. The calculated E_{rp} value is above 1 V vs standard hydrogen electrode (SHE), which lies within the transpassive dissolution range and precludes the occurrence of localized corrosion. This is in agreement with the experimental evidence that no localized corrosion is observed for this alloy in aerated seawater.

It is particularly important for the model to simulate the effect of chlorination because of its wide use in industry. Chlorination is used to eliminate biofouling, but the reduction of hypochlorite ions on the metal surface creates an additional cathodic process, which may increase the corrosion potential.[31-32] Figure 17 presents an analysis of the behavior of Alloy 254SMO in chlorinated seawater containing 7.62 ppm O_2 and 1 ppm Cl_2. Because of the presence of dissolved chlorine, the corrosion potential in this system is affected by the reduction of hypochlorite ions. The partial processes of the reduction of the $HClO_{aq}$ and ClO^- species are shown in Figure 17 by the dotted lines labeled as "E" and "F." Although the corrosion potential is increased as a result of the presence of hypochlorites, it is still substantially below the repassivation potential at 25°C. Thus, Alloy 254SMO is predicted to be resistant to localized corrosion even when it is in contact with seawater containing 1 ppm of dissolved chlorine. However, higher temperature will result in the lowering of the repassivation potential, which may give rise to localized corrosion of Alloy 254SMO. The temperature effect is shown in Figure 18, which has been generated for aerated seawater at 35°C. Figure 18 includes experimentally measured corrosion potential data, which are in agreement with the predicted value. In this case, the repassivation potential is reduced to 0.57 V_{SHE}, even though the temperature is increased by only 10°C. The corrosion potential is still below the repassivation potential,

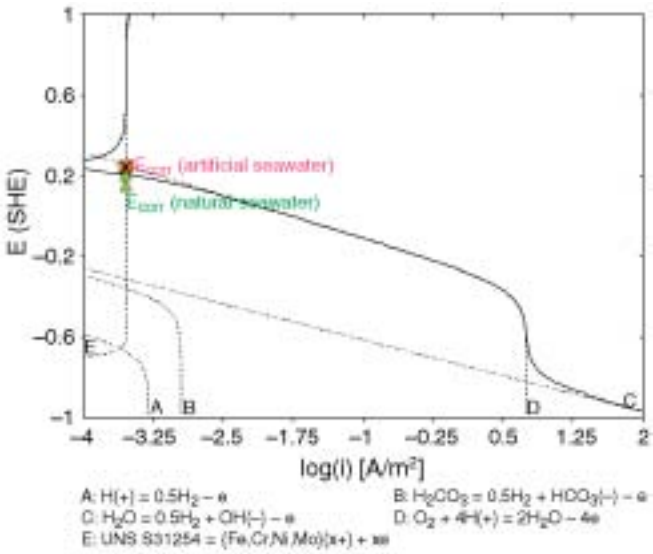

FIGURE 16. *Calculated current density vs potential relationship for Alloy 254SMO SS in aerated seawater at 25°C (7.62 ppm of dissolved O_2, rotation rate 1,000 rpm). The calculated corrosion potential is shown by the "x" symbol. The square and triangles show the experimental corrosion potentials in artificial seawater (7.62 ppm O_2) and natural seawater (6.8 ppm O_2), respectively.*

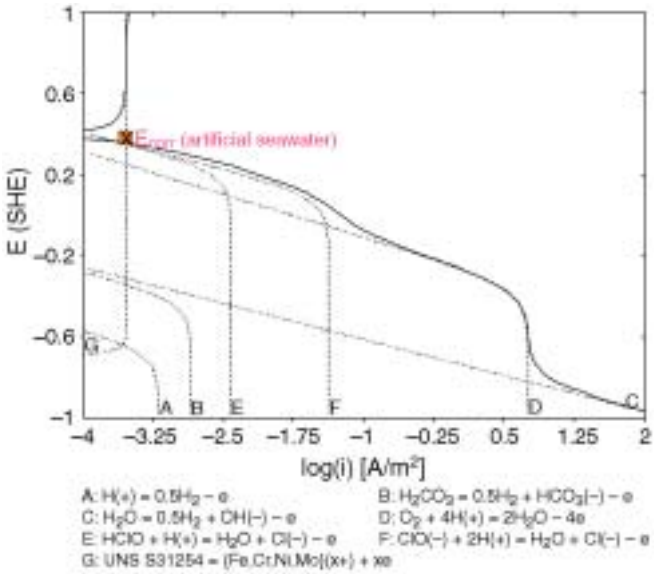

FIGURE 17. *Calculated current density vs potential relationship for Alloy 254SMO SS in chlorinated seawater containing 7.62 ppm O_2 and 1 ppm Cl_2 at 25°C (rotation rate 1,000 rpm). The calculated corrosion potential is shown by the "x" symbol. The square shows the experimental corrosion potential in artificial seawater.*

which indicates that there is still no tendency for localized corrosion.

A further increase in temperature leads to a decrease in the repassivation potential so that E_{rp} can drop below E_{corr}. According to model predictions, this occurs at 38°C to 39°C, depending on the level of chlorination. This is in agreement with practical experience, which indicates that Alloy 254SMO cannot be used in chlorinated seawater at temperatures above about 40°C.[36] Detailed modeling of the effect of temperature on repassivation potential will be presented in a future paper.

The behavior of aluminum in seawater environments is shown in Figures 19 through 21. Figure 19 shows the predicted current density vs potential relationship in aerated seawater (i.e., for the same conditions as those in Figures 14 and 16). In this case, calculations have been made for three rotation rates (i.e., 100, 1,000, and 2,500 rpm) because the anodic dissolution of aluminum in weakly alkaline solutions such as seawater is influenced somewhat by hydrodynamic conditions. In contrast to more corrosion-resistant metals such as Type 316L and Alloy 254SMO, the measured steady-state corrosion potential of aluminum does not reflect the reduction of oxygen molecules on a passive surface. Instead, it fairly rapidly drops to a value that results from localized corrosion. Therefore, the experimental corrosion potentials shown in Figure 19 (i.e., the square for artificial seawater and the triangles for natural seawater) lie fairly close to the repassivation potential. On the other hand, the calculated corrosion potential reflects

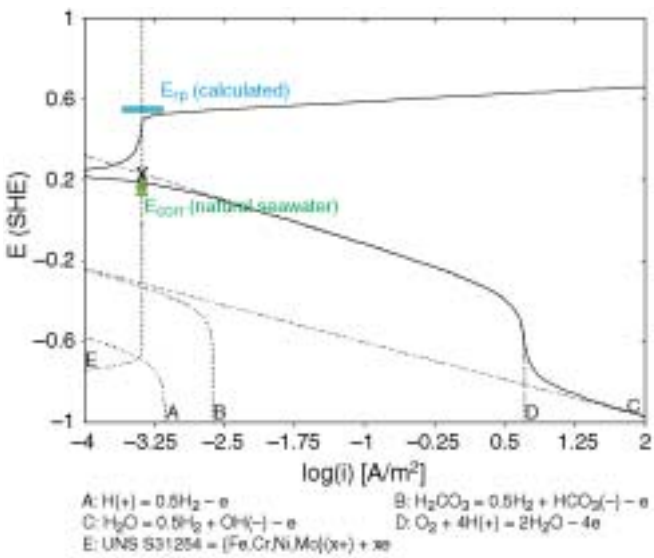

FIGURE 18. *Calculated current density vs potential relationship for Alloy 254SMO SS in aerated seawater containing 5.6 ppm O_2 at 35°C (rotation rate 1,000 rpm). The calculated corrosion potential is shown by the "x" symbol. The triangles show the experimental corrosion potential in natural seawater after 7 days and 14 days. The rectangle shows the calculated repassivation potential.*

the reduction of oxygen on an intact passive surface. Thus, the calculated corrosion potentials (marked by the "x" symbol) lie substantially above the experimental steady-state corrosion potential values as well as the repassivation potential. This represents the experimentally observed tendency of aluminum to undergo

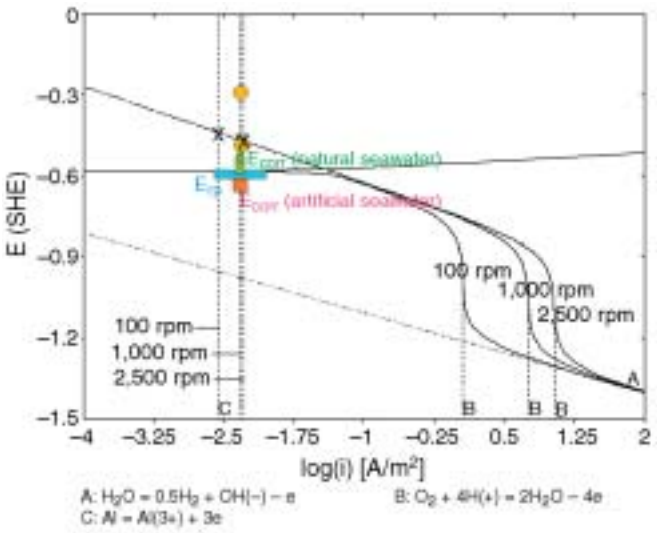

FIGURE 19. *Calculated current density vs potential relationship for aluminum in aerated seawater at 25°C (7.62 ppm of dissolved O_2) at various rotation rates. The calculated corrosion potentials are shown by the "x" symbol. The experimental repassivation potential is shown as a rectangle labeled E_{rp}. The square and triangles show the experimental steady-state corrosion potentials in artificial seawater (7.62 ppm O_2) and natural seawater (6.5 ppm O_2), respectively. Additionally, the circles show the results of short-term measurements of the corrosion potential at two rotation rates.*

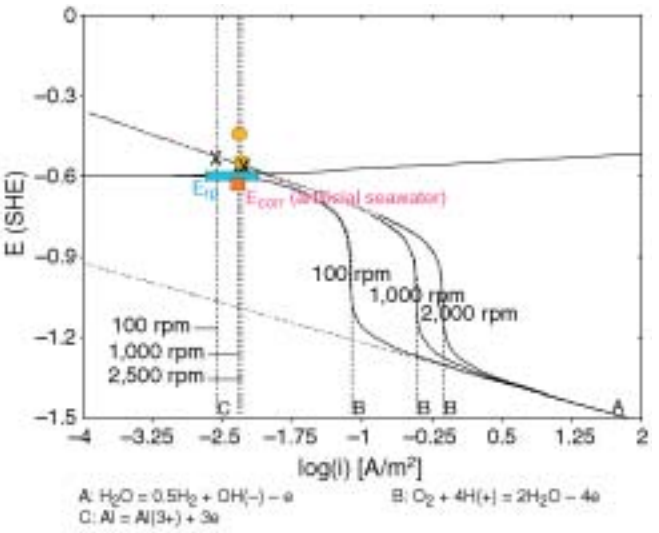

FIGURE 20. *Calculated current density vs potential relationship for aluminum in aerated seawater containing 0.38 ppm O_2 at 25°C and various rotation rates. The calculated corrosion potentials are shown by the "x" symbol. The experimental repassivation potential is shown as a rectangle labeled E_{rp}. The square shows the experimental steady-state corrosion potential in artificial seawater. The circles show the results of short-term measurements of the corrosion potential at two rotation rates.*

localized corrosion in aerated seawater. Although the steady-state experimental corrosion potential data are close to the repassivation potential, short-term measurements give higher values of the corrosion potential. The corrosion potentials obtained from short-term measurements are shown in Figure 19 as circles. These values, which are unavoidably scattered, provide an estimate of the corrosion potential on the surface of passive aluminum before the development of localized corrosion. The calculated corrosion potentials are in qualitative agreement with experimental data obtained from short-term measurements.

Figure 20 shows the behavior of the same system in which the concentration of dissolved oxygen has been reduced to 0.38 ppm. In this case, the reduced concentration of oxygen results in the lowering of the predicted corrosion potential. The experimental corrosion potentials obtained from short-term measurements are in qualitative agreement with the predicted ones. Despite the reduction in the dissolved oxygen concentration, the calculated corrosion potential is still above the repassivation potential, which indicates a tendency for localized corrosion. The experimental steady-state corrosion potential (cf. the square in Figure 20) reflects localized corrosion and does not differ from the one obtained in fully aerated solutions (Figure 19). The concentration of dissolved oxygen would have to be reduced below approximately 0.1 ppm for the corrosion potential to decline below the repassivation potential. Thus, no tendency for localized corrosion would be predicted for oxygen concentrations below ~0.1 ppm. This is in qualitative agreement with experimental data for seawater with low oxygen concentrations.[37] It should be noted that the cathodic kinetics exhibited in Figures 19 and 20 may be simplistic representations of the actual cathodic behavior of aluminum alloys. While the calculated cathodic reaction kinetics shown in Figure 19 may correspond reasonably well with experimental data on pure aluminum under some circumstances,[25] it does not account for the effect of surface condition that may result from prior anodic or cathodic polarization[25] or time of exposure at open-circuit potential (Figures 4 and 5). In the case of other aluminum alloys containing second-phase particles, the cathodic reaction kinetics on other phases may govern the overall cathodic kinetics of the alloy.[25,38] In such cases, the cathodic branch of the experimental polarization curve may not be represented accurately by the limiting current density for oxygen transport, which is assumed by the model.

Finally, Figure 21 shows the results of calculations for seawater with 8.41 ppm oxygen and 1 ppm chlorine. The additional cathodic process of ClO^- reduction increases the calculated corrosion potential from about –0.42 to –0.28 vs SHE. The elevation of the potential is in agreement with the short-term corrosion potential measurements and indicates an increased tendency for localized corrosion. If the chlorine concentration were reduced below approximately 0.1 ppm, no elevation in the corrosion potential would be predicted.

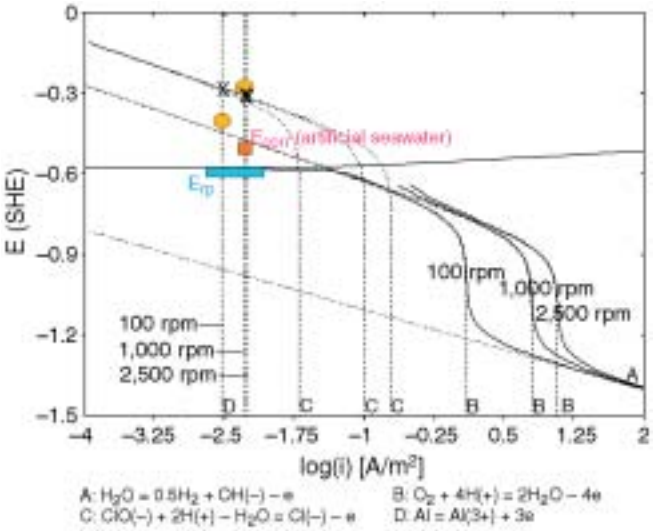

FIGURE 21. *Calculated current density vs potential relationship for aluminum in chlorinated seawater containing 7.66 ppm O_2 and 1 ppm Cl_2 at 25°C and various rotation rates. The calculated corrosion potentials are shown by the "x" symbol. The experimental repassivation potential is shown as a rectangle labeled E_{rp}. The square shows the experimental steady-state corrosion potential in artificial seawater. The circles show the results of short-term measurements of the corrosion potential at two rotation rates.*

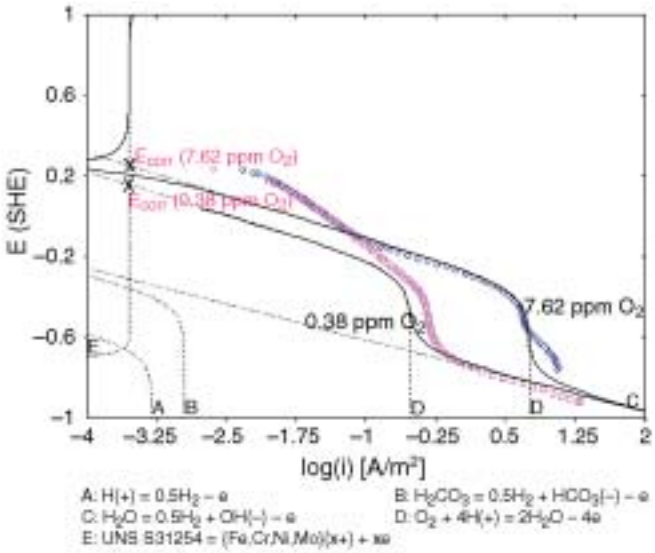

FIGURE 22. *Comparison of calculated and experimental cathodic polarization curves for Alloy 254SMO SS in artificial seawater at 25°C in solutions containing 7.62 ppm or 0.38 ppm O_2 (rotation rate 1,000 rpm).*

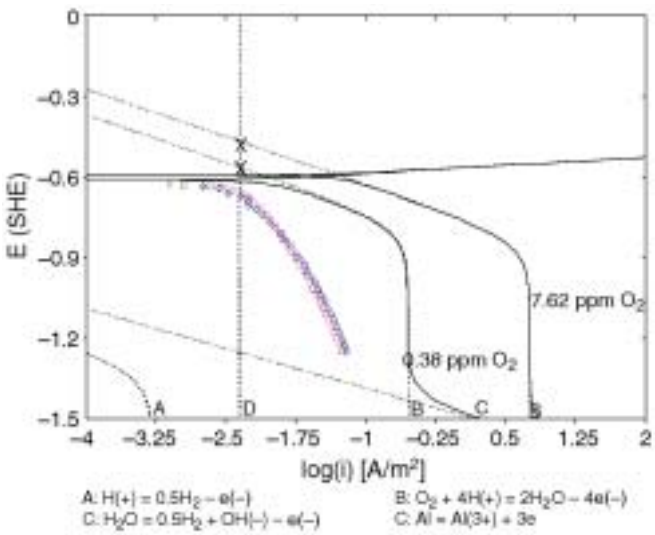

FIGURE 23. *Comparison of calculated and experimental cathodic polarization curves for Al 1100 in artificial seawater at 25°C in solutions containing 7.62 ppm or 0.38 ppm O_2 (rotation rate 1,000 rpm).*

In addition to verifying the model for predicting the corrosion potential, it is also worthwhile to compare predicted and experimental cathodic polarization curves. Such a comparison can be strictly valid only for artificial seawater since the model does not include the effects of biological activity, which strongly influence the oxygen reduction process. Figure 22 shows the calculated and experimental polarization curves for Alloy 254SMO in artificial seawater at two levels of dissolved oxygen, i.e., for 7.62 ppm and 0.38 ppm (rotating disk electrode, 1,000 rpm). For both oxygen concentration levels, the limiting current densities are very well predicted. Also, the Tafel portions of the cathodic curves that correspond to oxygen and water reduction are in good agreement with experimental data at potentials below ca. –0.05 V_{SHE}. Some deviations are observed at higher potentials as the corrosion potential is approached. This shift is due to the fact that the model predicts a low, steady-state corrosion current density in the passive state, whereas the measured corrosion potential corresponds to a somewhat higher current density. On the other hand, the model overpredicts the cathodic current densities on aluminum as illustrated in Figure 23. In contrast to model predictions, the experimental limiting current densities are not strong functions of dissolved oxygen concentration. As discussed above, this indicates that the cathodic branch of the polarization curve on aluminum is not controlled by simple diffusion-limited mass transport as implied by the model. However, this limitation of the model does not affect its usefulness for predicting the corrosion potential because the corrosion potential is controlled by the reduction of oxygen on passive surfaces at much lower current densities. Thus, the model remains valid in the current density ranges that correspond to passive dissolution (cf. Figures 12 and 13).

It should be noted that the modeling results reported here are strictly applicable only to artificial seawater. The model does not include the effects of biological activity in natural seawater, which are very significant for SS and typically manifest themselves

in large variations in the observed corrosion potential.[4-5,39] Such variations are important if the biological activity is not suppressed by chemical means such as chlorination. In general, the variations in the E_{corr} values necessitate a probabilistic treatment of the oxygen reduction process. These issues will be addressed in a future study. Also, a separate study addresses the development of a mechanistic model for calculating the repassivation potential as a function of solution chemistry.[40] This model has a wider applicability range than the correlations (Equations [2] through [4]), which only summarize the experimental results.

The model described in this paper does not consider crevice corrosion propagation. This will be treated in a separate paper. It is possible that under some conditions the growth of significant crevice corrosion may result in the lowering of corrosion potential[36] such that repassivation of crevice corrosion may occur. Such a result is not inconsistent with the present model, although it is not treated explicitly. Also, it should be noted that the model does not explicitly take into account the surface finish, which may influence the cathodic processes.[30] The model is generally valid for polished surfaces without any specific pretreatment. In principle, the effect of surface finish could be taken into account by altering the values of the exchange current densities. However, such an extension would not be practical because of a lack of relevant experimental data to calibrate model parameters and the inherent scattering of experimental data as a function of surface conditions.

CONCLUSIONS

❖ A methodology has been developed to predict the long-term occurrence of localized corrosion in seawater and similar aqueous environments. This methodology relies on comparing the values of the repassivation and corrosion potentials of a given alloy. Both potentials have been experimentally determined for Type 316L SS, Alloy 254SMO, and Al 1100 for selected combinations of environmental variables. The experimental data have been utilized to calibrate a computational framework that can predict the corrosion and repassivation potentials as functions of solution composition and temperature. For the corrosion potential, a mechanistic model has been established by combining a thermodynamic speciation module and an electrochemical module that takes into account the partial cathodic and anodic processes on a metal surface. The corrosion potentials calculated from the model are in agreement with experimental data. Unlike the corrosion potential, the repassivation potential is calculated using an empirical interpolation function. However, in a forthcoming paper, a new, mechanistic model will be developed for predicting the repassivation potential.

❖ The model and experimental results reported in this paper show that:

—The corrosion potential of Type 316L SS is typically more positive than its repassivation potential in seawater. This results in localized corrosion of Type 316L SS. Reduction in oxygen to less than 0.06 ppm is required to prevent localized corrosion. Chlorination further increases the corrosion potential and therefore exacerbates localized corrosion.

—The corrosion potential of Alloy 254SMO in natural and synthetic seawater is more negative than its repassivation potential, even in chlorinated seawater at 23°C. Thus, it would be expected to be resistant to localized corrosion.

—The corrosion potential of Al 1100 in natural and synthetic seawater is more positive than its repassivation potential and consequently aluminum would be expected to suffer localized corrosion.

❖ The combined model has been implemented in software that can be used as a convenient tool for analyzing the effect of environmental variables on localized corrosion.

ACKNOWLEDGMENTS

The work reported in this paper was funded by the National Institute of Standards and Technology Advanced Technology Program and co-sponsored by Chevron, DuPont, ExxonMobil, Mitsubishi Chemical, and Shell.

REFERENCES

1. Dechema Handbook of Corrosion, vol. 11 (Weinheim, NY: VCH Publishers, 1992), p. 66.
2. S. Motoda, Y. Suzuki, T. Shinohara, S. Tsujikawa. Corros. Sci. 31 (1990): p. 515.
3. J.P. Audouard, C. Compere, N.J.E. Dowling, D. Feron, D. Festy, A. Mollica, T. Rogne, V. Scotto, U. Steinsmo, C. Taxen, D. Thierry, "Effect of Marine Biofilms on Stainless Steels—Results from a European Exposure Program," 1995 Int. Conf. on Microbially Influenced Corrosion, paper no. 3 (Houston, TX: NACE International, 1995).
4. G. Salvago, L. Magagnin, Corrosion 57 (2001): p. 680.
5. G. Salvago, L. Magagnin, Corrosion 57 (2001): p. 759.
6. A. Mollica, A. Travis, E. Traverso, G. Ventura, G. de Garolis, R. Dellepiane, Corrosion 45 (1989): p. 48.
7. U. Steinsmo, T. Rogne, J. Drugli, Corrosion 53 (1997): p. 955.
8. E.B. Shone, R.E. Malpas, P. Gallagher, "Stainless Steels as Replacement Materials for Copper Alloys in Seawater Handling Systems," Institute of Marine Engineers Presentation (read April 5, 1988).
9. M. Schumacher, Seawater Corrosion Handbook (Park Ridge, NJ: Noyes Data Corp., 1979).
10. H.M. Shalaby, A. Husain, Br. Corros. J. 27 (1992): p. 45.
11. A.I. Asphahani, P.E. Manning, W.L. Silence, F.G. Hodge, Highly Alloyed Stainless Materials for Seawater Applications, Technical Report (Kokomo, IN: Haynes International, 1989).
12. T.S. Lee, A.H. Tuthill, "Guidelines for the Use of Carbon Steel to Mitigate Crevice Corrosion of Stainless Steel in Seawater," CORROSION/82, paper no. 63 (Houston, TX: NACE, 1982).
13. R.M. Kain, "Seawater Testing to Assess the Crevice Corrosion Resistance of Stainless Steels and Related Alloys," 12th Int. Corros. Cong., vol. 3B (Houston, TX: NACE, 1993), p. 1,889.
14. M.A. Streicher, Mater. Perform. 22 (1983): p. 37.

15. J.A. Oldfield, "Corrosion Initiation and Propogation of Nickel-Based Alloys in Severe Seawater Applications," CORROSION/95, paper no. 266 (Houston, TX: NACE, 1995).
16. O. Strandmyr, O. Hagerup, "Field Experience with Stainless Steel Materials in Seawater Systems," CORROSION/98, paper no. 707 (Houston, TX: NACE, 1998).
17. P.O. Gartland, "Modeling of Crevice Processes," Research Topical Symp., Crevice Corrosion: The Science and its Control in Engineering Practice, CORROSION/96 (Houston, TX: NACE, 1996).
18. D.S. Dunn, G.A. Cragnolino, N. Sridhar, Corrosion 56 (2000): p. 90.
19. W. Baptista, G. Pimenta, Mater. Perform. 34 (1995): p. 29.
20. S. Valen, R. Johnsen, P.O. Gartland, J.M. Drugli, "Seawater Piping Systems Designed with AISI 316 and RCP Anodes," CORROSION/99, paper no. 321 (Houston, TX: NACE, 1999).
21. T.J. Lennox, M.H. Peterson, C.W. Billow, Mater. Perform. 22 (1983): p. 49.
22. A.J. Sedriks, Int. Met. Rev. 27 (1982): p. 321.
23. M.L. Berndt, "Thermal Spray Coatings," in Corrosion: Fundamentals, Testing, and Protection, ASM Handbook, vol. 13A (Materials Park, OH: ASM International, 2003), p. 803.
24. S. Furuya, N. Soga, Corrosion 46 (1990): p. 989.
25. R. Gundersen, K. Nisancioglu, Corrosion 46 (1990): p. 279.
26. A. Anderko, R.D. Young, Corrosion 56 (2000): p. 543.
27. A. Anderko, P. McKenzie, R.D. Young, Corrosion 57 (2001): p. 202.
28. H. Kaesche, Werkst. Korros. 14 (1963): p. 557.
29. H.L. Craig, J.R. Scott, J. Mater. 4, 3 (1969): p. 540-555.
30. N. Le Bozec, C. Compere, M.L'Her, A. Laouenan, D. Costa, P. Marcus, Corros. Sci. 43 (2001): p. 765.
31. J.-K. Wu, J. Electrochem. Soc. 134 (1987): p. 1,462.
32. B. Gaur, A.K. Singh, N.J. Rao, Indian J. Chem. Technol. 1 (1994): p. 225.
33. A. Anderko, N.S. Sridhar, "Corrosion Simulation for the Process Industry," CORROSION/2001, paper no. 01348 (Houston, TX: NACE, 2001).
34. H.P. Leckie, Corrosion 24 (1968): p. 70.
35. L. de Micheli, C.A. Barbosa, A.H.P. Andrade, S.M.L. Agostinho, Br. Corr. J. 35 (2000): p. 297
36. S. Valen, P.O. Gartland, U. Steinsmo, "Long Duration Tests of the Crevice Corrosion Rate of High-Alloyed Stainless Steels in Seawater," CORROSION/93, paper no. 496 (Houston, TX: NACE, 1993).
37. E.D. Verink, Jr., P.F. George, Mater. Perform. 12, 5 (1973): p. 26.
38. G.O. Ilevbare, J.R. Scully, Corrosion 57 (2001): p. 134.
39. B. Little, R. Ray, P. Wagner, Z. Lewandowski, W.C. Lee, W.G. Characklis, F. Mansfeld, Biofouling 3 (1991): p. 45.
40. A. Anderko, N. Sridhar, D.S. Dunn, Corros. Sci. 46 (2004): p. 1,583-1,612.
41. J.F. Zemaitis, Jr., D.M. Clark, M. Rafal, N.C. Scrivner, Handbook of Aqueous Electrolyte Thermodynamics (New York, NY: American Institute of Chemical Engineers [AIChE], 1986), p. 852.
42. M. Rafal, J.W. Berthold, N.C. Scrivner, S.L. Grise, "Models for Electrolyte Solutions," in Models for Thermodynamic and Phase Equilibria Calculations, ed. S.I. Sandler (New York, NY: Marcel Dekker, 1995), p. 601-670.
43. J.C. Tanger, H.C. Helgeson, Am. J. Sci. 288 (1988): p. 19.
44. E.L. Shock, H.C. Helgeson, Geochim. Cosmochim. Acta 52 (1988): p. 2,009.
45. E.L. Shock, H.C. Helgeson, Geochim. Cosmochim. Acta 54 (1990): p. 915.
46. D.A. Sverjensky, Rev. Mineral. 17 (1987): p. 177.
47. L.A. Bromley, AIChE J. 19 (1973): p. 313.
48. K.S. Pitzer, J. Phys. Chem. 77 (1973): p. 268.
49. G. Soave, Chem. Eng. Sci. 27 (1972): p. 1,197.
50. H.P. Meissner, "Thermodynamics of Aqueous Systems with Industrial Applications," in Am. Chem. Soc. Symp. Ser. 133, ed. S.A. Newman (Washington, DC: American Chemical Society, 1980), p. 495.
51. A. Anderko, M.M. Lencka, Ind. Eng. Chem. Res. 37 (1998): p. 2,878.
52. M.M. Lencka, A. Anderko, S.J. Sanders, R.D. Young, Int. J. Thermophys. 19 (1998): p. 367.
53. Shatalov, Dokl. Akad. Nauk SSSR 86 (1952): p. 775.
54. J.E. Draley, W.E. Ruther, Corrosion 12 (1956): p. 441t.
55. K.F. Lorking, J.E.O. Mayne, J. Appl. Chem. 11 (1961): p. 170.
56. M.J. Pryor, D.S. Keir, J. Electrochem. Soc. 105 (1958): p. 629.
57. A.M. Beccaria, G. Poggi, Corrosion 42 (1986): p. 470.
58. S.M. Moon, S.-I. Pyun, Corrosion 54 (1998): p. 546.
59. A.A. Adams, R.T. Foley, Corrosion 31 (1975): p. 84.
60. K.H.M. Kamel, S.A. Awad, A. Kassab, J. Electroanal. Chem. 99 (1979): p. 121.
61. S.I. Pyun, S.-M. Moon, S.-H. Ahn, S.-S. Kim, Corros. Sci. 41 (1999): p. 653.

APPENDIX A

A thermodynamic model for calculating speciation, phase, and chemical equilibria in aqueous solutions has been described in detail by Zemaitis, et al.,[41] and Rafal, et al.[42] Here, we briefly describe the essential features of the model.

A multicomponent system can be fully characterized if the standard-state properties of all species and the solution nonideality (as exemplified by species activities) are known. These properties make it possible to compute the partial molal Gibbs energy of the i-th species, i.e.:

$$\overline{G}_i = \overline{G}_i^{\,0} + RT \ln m_i \gamma_i \qquad \text{(A-1)}$$

where $\overline{G}_i^0$ is the standard-state partial Gibbs energy and γ_i is the activity coefficient. Thus, the thermodynamic properties of the system can be calculated if the standard-state Gibbs energies are available for all species as functions of temperature and pressure (i.e., $\overline{G}_i^0$ [T,P] and the activity coefficients are known as functions of the composition vector, m, and temperature (i.e., γ_i[m,T]).

The key to representing the standard-state properties over substantial temperature and pressure ranges is the accurate knowledge of the heat capacity and volume. For this purpose, the Helgeson-Kirkham-Flowers-Tanger[43] (HKFT) equation of state is used. This equation accurately represents the standard-state thermodynamic functions for aqueous, ionic, or neutral species as functions of both temperature and pressure. In its revised form,[43] the HKFT equation is capable of reproducing the standard-state properties up to 1,000°C and 5 kbar.

If the HKFT equation parameters are not available from the regression of experimental data, they can be estimated. For this purpose, Shock and Helgeson[44-45] presented correlations for most solution species except for complexes. Sverjensky[46] developed an estimation method for several classes of complexes. In addition to the HKFT equation parameters, these methods make it possible to predict the reference-state enthalpy and entropy if the reference-state Gibbs energy is known. These and other estimation techniques have been reviewed in detail by Rafal, et al.[42]

The activity coefficient model used for representing the solution nonideality is an extended form of an expression developed by Bromley.[47] The Bromley equation is a combination of the Debye-Hückel term for long-range electrostatic interactions and a semi-empirical expression for short-range interactions between cations and anions. In a multicomponent system, the activity coefficient of an ion, i, is given by:

$$\log \gamma_i = \frac{-Az_i^2 I^{1/2}}{1+I^{1/2}} + \sum_j^{NO}\left[\frac{|z_i|+|z_j|}{2}\right]^2 \left[\frac{(0.06+0.6B_{ij})|z_i z_j|}{\left(1+\frac{1.5}{|z_i z_j|}I\right)^2} + B_{ij} + C_{ij}I + D_{ij}I^2\right] m_j \quad \text{(A-2)}$$

where A is the Debye-Hückel coefficient that depends on temperature and solvent properties, z_i is the number of charges on ion i, I is the ionic strength (i.e., $I = 0.5\sum z_i^2 m_i$), NO is the number of ions with charges opposite to that of ion i, and B_{ij}, C_{ij}, and D_{ij} are empirical, temperature-dependent cation-anion interaction parameters. Bromley's[47] original formulation contains only one interaction parameter, B_{ij}, which is sufficient for systems with moderate ionic strength. For concentrated systems, the two additional coefficients C_{ij} and D_{ij} usually become necessary. The three-parameter form of the Bromley model is capable of reproducing activity coefficients in solutions with ionic strength up to 30 mol/kg. The temperature dependence of the B_{ij}, C_{ij}, and D_{ij} parameters is usually expressed using a simple quadratic function.

The Bromley model is restricted to interactions between cations and anions. For ion-molecule and molecule-molecule interactions, the well-known model of Pitzer[48] is used. To calculate the fugacities of components in the gas phase, the Redlich-Kwong-Soave[49] equation of state is used. In the absence of sufficient experimental data, reasonable predictions can be made using a method developed by Meissner,[50] which makes it possible to extrapolate the activity coefficients to higher ionic strengths based on only a single, experimental or predicted, data point.

Once the speciation of the solution is obtained from the thermodynamic model, transport properties are calculated from separate models. In particular, diffusivity of species is computed from the model of Anderko and Lencka[51] and viscosity is obtained from the model of Lencka, et al.[52]

LIST OF SYMBOLS

a_i activity of species i in the bulk
a_i^* activity of species i at the surface
E_{corr} corrosion potential
E_i^0 equilibrium potential as calculated from the Nernst equation for a reaction involving species i
E_{rcrev} repassivation potential from crevice corrosion measurements
E_{rp} repassivation potential
F Faraday constant
$\bar{G}_i$ partial molal Gibbs energy of species i
$\bar{G}_i^0$ standard-state partial molal Gibbs energy of species i
i^0 exchange current density
i_j current density for a reaction involving species j (j = Me, H_2O, O_2, etc.)
$i_{j,lim}$ limiting current density related to the transport of species j
i_j^* reaction rate constant (a concentration-independent part of exchange current density)
i_{Me} current density that leads to the formation of metal ions in solution
i_{MeO} current density that leads to the formation of an oxide layer
i_p passive current density
$i_{p,j}$ component of the passive current density due to a reaction with species j
I ionic strength
k_j kinetic rate constant for a reaction involving species j
k_m mass-transfer coefficient
K_j equilibrium constant for the formation of a surface complex with species j
l_j reaction rate for the dissolution of a surface complex with species j
m_j molality of species j
PRE pitting resistance index
q reaction order
r reaction order
s reaction order
t time
T temperature
u reaction order
v reaction order
z charge

Greek Symbols

a electrochemical transfer coefficient
γ_j activity coefficient of species j
θ_p fraction of surface covered by a passive film